Surface Pressure Measurements for CFD Code Validation in Hypersonic Flow

William L. Oberkampf, Daniel P. Aeschliman, John F. Henfling, and Donald E. Larson
Sandia National Laboratories
Albuquerque, NM 87185-0825

Abstract

Extensive surface pressure measurements were obtained on a hypersonic vehicle configuration at Mach 8. All of the experimental results were obtained in the Sandia National Laboratories Mach 8 hypersonic wind tunnel for laminar boundary layer conditions. The basic vehicle configuration is a spherically blunted 10° half-angle cone with a slice parallel with the axis of the vehicle. The bluntness ratio of the geometry is 10% and the slice begins at 70% of the length of the vehicle. Surface pressure measurements were obtained for angles of attack from -10 to $+18^O$, for various roll angles, at 96 locations on the body surface. A new and innovative uncertainty analysis was devised to estimate the contributors to surface pressure measurement uncertainty. Quantitative estimates were computed for the uncertainty contributions due to the complete instrumentation system, nonuniformity of flow in the test section of the wind tunnel, and variations in the wind tunnel model. This extensive set of high-quality surface pressure measurements is recommended for use in the calibration and validation of computational fluid dynamics codes for hypersonic flow conditions.

DISCLAIMER

Portions of this document may be illegible in electronic image products. Images are produced from the best available original document.

Nomenclature

d_b Diameter of the model base
L   Model length
M_∞ Freestream Mach number
p   Body surface pressure
p_0 Total pressure
p_∞ Freestream static pressure
q_∞ Freestream dynamic pressure
r_b Radius of the model base
Re_L Freestream Reynolds number based on body length
Re_{r_n} Freestream Reynolds number based on nose radius
Re_∞ Freestream Unit Reynolds number, ft^{-1}
r_n Radius of the nose
T_0 Total temperature
T_w Model wall temperature
x   Axial distance measured from the nose
α Angle of attack, positive for slice on windward side
δ Flap deflection angle, ($\delta = 0^o$ for the slice-only geometry)
θ_c Model cone half-angle
ϕ Model roll angle, $\phi = 0^o$ for slice on windward side at positive α

I. Introduction

Over the years a number of fundamental experiments have been conducted on simple vehicle shapes, such as sharp or spherically blunted cones, in hypersonic flow [1-6]. These experiments were conducted twenty to thirty years ago when the emphasis was on understanding the basic flow physics and obtaining data bases for the evaluation of approximate analytical techniques. Of these experiments conducted in the 1960's and early 70's, probably the most used today for CFD validation are those by Tracy [1] and Stetson [6]. Tracy measured surface pressure, heat transfer, and pitot-pressure throughout the flow field of a sharp cone with half-angle of 10°. The freestream Mach number was nominally 8 and the Reynolds numbers (based on model length) were 0.24 and 0.48 x 10^6. Stetson [6] measured surface pressure, pitot-pressure surveys, and surface oil flow patterns on sharp and blunt cones with a half-angle of 5.6^o. The freestream Mach number was 14.2 and the Reynolds number (based on sharp cone length) was 0.79 x 10^6. For both experiments the boundary layer over the length of the body, for all angles of attack, was laminar, thereby providing well understood viscous flow. Although both of these experiments are classic experiments, they do not meet the detailed CFD information and uncertainty analysis requirements.

One of the key elements in high quality and effective code validation experiments is clear definition from the onset that the experiment will only be a computational fluid dynamics (CFD) code validation experiment. In a CFD code validation experiment the model geometry is optimized for code validation, not flight vehicle requirements, the highest quality fabrication techniques are used, flow conditions and CFD required boundary conditions are specifically measured, and instrumentation uncertainty is rigorously examined. Designers of validation experiments must develop a better understanding of the detailed assumptions made in the numerical simulation so that experiments can be designed to match these assumptions as closely as possible. For example, in choosing a body geometry for a validation experiment, a configuration should be chosen that

eliminates unnecessary numerical difficulties or geometrical complexities. From the perspective of a flight vehicle designer, the optimum validation geometry would probably have unrealistic or unworkable features for a flight vehicle. In a validation experiment, however, these views must not be allowed to compromise the geometry.

Over the last several years, Sandia National Laboratories has conducted a research effort, referred to as the Joint Computational-Experimental Aerodynamics Program (JCEAP), for the dual purposes of CFD code validation, and improvement of the quality of high-speed wind tunnel experimentation. The research program was designed and executed so that both computational and experimental capabilities would benefit from the potential synergisms inherent in closely coupled computational and experimental research. The merits of this approach have been demonstrated and documented [7-10] for the first phase of the program, a study of aerodynamic forces and moments on a hypersonic research vehicle configuration. In Phase One, extensive force and moment measurements, supported by a comprehensive uncertainty analysis, were compared to code predictions for laminar flow conditions. The model geometry chosen was a 10° half-angle cone with a spherical nose with 10% bluntness and an aft slice parallel to the cone axis. To the slice could be attached flaps of varying angle, 10, 20, and 30°. The model geometry with varying flap angles, angles of attack, and laminar flow, perfect gas conditions, produces flow physics ranging from relatively simple to highly complex.

The second phase of JCEAP is addressing the next level of difficulty in code validation and experimentation; measurement of surface pressure distributions on an identically sized and shaped model at the same nominal flow conditions. Accurate CFD prediction of surface pressure measurements demands a higher level of numerical simulation fidelity than the prediction of body forces and moments. Similarly, the difficulty and level of detail required by the experimental surface pressure measurements is much more demanding that the previous force and moment measurements. Although surface pressure measurements are not generally considered to require state-of-the-art techniques, very accurate, low pressure measurements in a hypersonic wind tunnel have proven to be challenging. Also during the research program, an experimental uncertainty analysis procedure was devised that permits the most detailed estimate of uncertainty sources yet devised for wind tunnel experiments.

In this paper, an experiment is described and surface measurements are presented for the JCEAP hypersonic vehicle configuration at Mach 8. All of the results were obtained in the Sandia National Laboratories long-duration, blowdown, hypersonic wind tunnel. Pressures were measured at 96 locations on the model surface, with roughly one-third of these located in the slice/flap region. This paper presents only the pressure measurements for the slice-only configuration; no deflected-flap pressure measurements are presented. An extensive uncertainty analysis was conducted to estimate quantitatively the accuracy of the measurements. The innovative uncertainty analysis was able to quantitatively estimate the individual contributions to system level instrumentation, test section flow field nonuniformity, and model geometry variations. The results of this experiment provide extensive surface pressure measurements for validation of CFD codes in laminar, perfect gas, flow conditions.

II. Experimental Apparatus and Procedure

Wind Tunnel

The Sandia National Laboratories blowdown-to-vacuum hypersonic wind tunnel consists of

three contoured axisymmetric nozzles, arranged like a Gatling gun around a common hub. The test section Mach numbers are nominally 5, 8, and 14, respectively. Each nozzle is provided with its own electric resistance heater to prevent flow condensation in the test section. Mach 8 operation uses dry nitrogen, and the total pressure, p_0, is variable from 250 to 1000 psia. Depending on electrical heating and nitrogen flow rate, total temperature, T_0, can be varied from 950 to 1650 R. The available ranges of p_0 and T_0 provide a unit freestream Reynolds number, Re_∞, range of 0.8 to 6.2 million/ft. During a run the total pressure is manually controlled, but all other operating parameters are automatically controlled through a Hewlett-Packard 1000 F-series computer. Usable run times are typically 30-60 seconds, depending on flow Reynolds number, and turnaround time between runs is one hour or less.

The Mach 8 test section has a diameter of 14 in. and is provided with 8 x 15-in. schlieren-grade windows on the top, bottom, and sides. The windows provide access for a variety of optically-based flow diagnostics. Model pitch angle (angle of attack) is varied using a computer-controlled arc-sector drive, but the drive does not have a feedback control system. As a result, the angles of attack attained deviated from the commanded values by up to a few tenths of a degree. Model roll angle and configuration modifications are easily changed between runs by retracting the aft portion of the test section. Figure 1 shows an overall view of the wind tunnel with the test section open.

Wind Tunnel Model

The model geometry is a 10.391 in. long, 10% spherically blunted cone with a slice on one side of the body (see Fig. 2). The slice is parallel to the axis and begins at 0.7 of the length of the body, measured from the spherical nose tip. The model was designed so that three different flaps could be attached to the aft portion of the slice, providing deflection angles of 10, 20, and 30°. The trailing edge of the flap extended completely to the base of the body for every flap angle. This was done to simplify the body geometry and outflow boundary conditions at the base for a CFD simulation.

The model is constructed of annealed Invar 36 low-expansion alloy to minimize distortion due to asymmetric heating at high angle of attack. Figure 3 shows a longitudinal cross-section of the model, and the adjacent portion of the base cover and sting, and the sting cover. The model was constructed in four sections (plus detachable nose tips) to permit machining operations and the installation of steel pressure port inserts during fabrication. This design approach also greatly facilitated tubing connections between ports and internally mounted pressure modules during subsequent model assembly. The fourth (aft) section, which includes the slice, was constructed in two parts to allow the extensive inner-surface machining required, then oven-brazed together prior to final machining and grinding. The center aft portion of the slice is the location of the flaps and is removable. The aft stage is also provided with an O-ring for each matching pressure port in the flap assemblies. Final grinding of the outer contour was performed with all sections assembled, the zero-degree flap section installed, and with alignment pins and centering O-rings in place. A screw-driven wedge assembly with access from the rear of the model is used to pull the flaps down firmly against the O-rings. A detailed inspection of the model and pressure port locations was conducted following final model fabrication. This inspection report is documented in Ref. 11.

A total of 96 pressure ports were machined in the model surface; each pressure orifice had a diameter of 0.029 in. Fifteen axial stations were fabricated with pressure orifices. Three axial stations on the cone, 3.2, 5.2, and 7.2 in. from the nose, were heavily instrumented (Figs. 4a-4c). Each of these stations had 16 orifices. The remaining extensively instrumented section of the model

was in the slice/flap region (Fig. 5). In this region were 40 orifices.

The model is supported in the tunnel by a stiff aft sting constructed of 15-5PH maraging steel. Angle of attack correction for sting deflection under aerodynamic loading was included in all data. The maximum sting deflection correction was 0.08° for a flap angle of 30°, a roll angle of 0°, and an angle of attack of 18°. A base cover extension of 3.600 in. OD and length of 0.625 in. was fabricated as part of the sting and provided the attachment point to the model (see Fig. 6). The extension has a flat on one edge to conform to the slice on the model, and a hollow recess which provided additional volume for the pressure tubing.

A cylindrical section covering the sting was fabricated and attached to the sting (Fig. 6). The cylindrical section covered pneumatic tubing controlling the pressure module switching and the pressure module cables. More importantly, however, it provided a mathematically-definable and repeatable geometry for the base region of the model. For certain model angle of attack and flap conditions it is likely that recirculating flow from the base region may influence the pressure distribution on the model surface. For CFD modeling purposes, this geometry must be accurately known, easily definable, and must be repeatable from run-to-run. This sting cover is another example of simplifying the geometric design in a validation experiment to eliminate unnecessary complexity.

Instrumentation

The model internal geometry allows installation of two 48-port Pressure Systems, Inc. (PSI) "Slimline" electronically scanned pressure (ESP) modules. A 0.36 psid full scale output module and a 1.0 psid module were positioned side-by-side in the aft section of the model. During the last decade researchers at NASA Langley Research Center [12-14] and Pressure Systems, Inc. [15]) have pioneered the development of electronically-scanned pressure instrumentation. Their work has substantially improved accurate surface pressure measurements on multiport models at the low freestream static pressures representative of typical hypersonic wind tunnels. We have incorporated many of the NASA Langley and PSI staff suggestions and procedures in the present program. Figure 7 shows the model during module installation after one module had been installed.

The model incorporated four Med-therm, Inc. Model TCS-E-10370, 0.060-in. OD coaxial Type E thermocouples mounted in the model wall on the windward and leeward rays, at axial locations x=3.00 in. and 9.10 in., respectively. The thermocouples provided model surface temperature for input boundary conditions required for the CFD calculations. A Type T thermocouple was attached to the case of one of the ESP modules to measure module temperature during a run. Model surface temperature at four locations and the pressure module temperature were recorded for each angle of attack for each run.

Since the ESP modules are differential devices, in order to measure absolute pressure, a good vacuum reference (10E-4 psia) was essential for the zero reference side of the modules. Zero reference pressures near 10E-5 psia at the modules were achieved through a combination of high vacuum pumping capacity, minimum leakage and outgassing, and adequate tubing conductance. Particular attention was paid to minimizing leaks, since even a minute leak will cause major problems at these low pressures. A temperature-stabilized MKS Baratron 100 torr (absolute) Capacitance Displacement Gage (CDG) was used in place of the standard quartz bourdon gage internal to the pressure control unit to achieve the desired calibration accuracy. The zero reference lines were continuously evacuated and the calibration line was kept evacuated, except during the

actual calibration procedure. The modules were always switched to the calibrate position immediately prior to tunnel shutdown in order to avoid high dynamic overloads on the individual sensor elements.

The ESP modules were calibrated immediately prior to each tunnel run with the tunnel evacuated to 0.06 psia or below. This approach was used to ensure the module heat transfer characteristics, and thus temperature, were the same during calibration and test. As noted above, the module case temperature was monitored and recorded; module temperature was observed to achieve a new stable equilibrium temperature after a few minutes once the tunnel was evacuated. Module temperature was observed to be constant to within 0.1R over the entire period from the initiation of the calibration procedure, to the completion of a tunnel run. Additional details of the pressure measurement system and experimental procedure is described in Ref. 11 and 16.

The overriding consideration in the development of the model surface pressure measurement system was the pressure lag time (also commonly referred to as settling time) of the 0.040 in. ID, Nylon tubing connecting the model surface pressure ports to the pressure transducers. A previous investigation of base pressure lag time using long (10 ft) tubing and up to five pressure transducers located outside the tunnel [10] had shown lag times of up to 3 seconds to stabilize. Pressure lag times of this magnitude were unacceptable for obtaining many angles of attack during one run.

To determine the actual lag characteristic of each port for the nominal tunnel flow conditions, the model was pitched, in separate runs, to positive and negative 10° angle of attack, while pressure data were recorded for each of the 96 ports. Data were also recorded at the maximum data sampling rate of 10 kHz for all ports to determine pressure lag time. Typical pressure lags were 0.05-0.10 sec to achieve a stable pressure within 0.1% of the final value. The largest lag time observed, 0.3 sec, occurred at one of the ports on the slice. To be conservative, a delay time of 0.5 sec was used prior to recording pressure data following each change to a new angle of attack during data acquisition runs. Observed lag times were consistent with predictions based on the analysis of McKee [17].

Experimental Conditions

As this experiment was designed to be a code validation experiment, it was important that the state of the boundary layer was known with confidence. In previous work [7,10], liquid crystals were applied to the surface of the model to determine whether the boundary layer was laminar or turbulent. It was conclusively shown that for a Reynolds number of 1.80×10^6, based on model length, laminar flow was assured over the full length of the vehicle for all angles of attack.

Table 1 summarizes the mean wind tunnel test conditions during the experiment. Some random variation in test conditions occurred from run-to-run. These were due to variations in setting and controlling wind tunnel stagnation and freestream conditions. Also shown in Table 1 is the standard deviation of the parameter and the percentage of the mean value the standard deviation represents.

Pressure measurements were made at twelve separate angles of attack, α, during each run; angle of attack varied from -9 to 18°. The sequence of nominal angle of attack during a run was 0, -9, -6, -3, 0, 3, 6, 9, 12, 15, 18, and 0°. For each of these α's, the roll angle was set at 0 (slice on the windward side), 90, 180, and 270°. In addition, pressure measurements were made with the model at two different axial locations in the test section, 7.6 in. and 4.1 in. The forward axial location, 7.6 in., places the model essentially at the center of rotation of the pitching strut. As a

result, the model rotates about the x/L = 0.4 body station during an angle of attack sweep at the forward axial station. At the aft axial station, the model rotates and translates downward in the test section for negative angles of attack; conversely, it rotates and translates upward for positive α's. Roughly 55,000 surface pressure measurements were obtained during the experiment.

Listed in Table 2 is a complete run schedule for the experiment. A number of features in the run schedule can be seen that are unusual from the traditional perspective of a wind tunnel experiment. First, repeat runs were scheduled and executed for almost every configuration; one configuration had three repeat runs. The purpose for this is to obtain a large number of multiple data sets with which to conduct an extensive uncertainty analysis. Second, noting that the run number reflects the chronological order, it can be seen that for $\delta = 0^\circ$, repeat runs were made substantially later during the experiment. For example, Run 20 and Run 62 were made nearly four weeks apart. Comparing these two runs, as opposed to comparing two runs on the same day, aids in estimating the overall measurement system repeatability. The time span from Run 20 to the last run of the experiment, Run 133, was eight weeks. Third, a substantial number of runs for each configuration were made at the aft axial tunnel station. By comparing the pressure measurements between the forward and aft stations one can quantitatively estimate the effect of changes in the test section flow field.

III. Uncertainty of Measurements

In surveying the literature documenting a wide variety of wind tunnel experiments, one rarely finds an analysis conducted to quantify the uncertainty of the measurements. It is becoming more common that estimates of experimental uncertainty are quoted by the researcher, but a rigorous and detailed explanation of how these estimates were obtained is normally lacking. Many times this lack of a detailed uncertainty analysis is justified because of the press of time or budget constraints. In experiments designed to validate CFD codes, however, the present authors strongly believed this is unacceptable.

Typical uncertainty analyses consider the repeatability of individual instrumentation components such as freestream conditions in the test section, strain gages, and pressure transducers [18]. It is clear from using this type of procedure that certain important factors contributing to measurement uncertainty are not included: for example, interaction of various instrumentation components, uncertainty in angular settings of the model in the test section, and uncertainty due to freestream flow nonuniformities. An innovative procedure was devised for quantitatively estimating these types of uncertainties and was first described in Refs. 19. The procedure was used to quantify the total uncertainty of force and moment measurements on the same model geometry as used in the present experiment. The current effort further develops the procedure to include a method for estimating uncertainties due to imperfections of the wind tunnel model. The procedure for statistically estimating these uncertainty components is based on the idea of comparing measurements obtained from certain types of repeat runs, runs with the model at different locations in the test section, and use of symmetry features of the model geometry. To take full advantage of this new procedure special attention must be given to constructing the run schedule to maximize information used in the analysis.

The analysis procedure developed is able to delineate experimental uncertainty in pressure measurements caused by three separate sources: total system instrumentation and model alignment, test section flow field nonuniformity, and model geometry. This analysis is an experimentally based statistical estimate of variance components of surface pressure measurements. The elements

in each of these uncertainties will now be discussed and the calculation procedure will be described.

System Instrumentation and Model Alignment Uncertainty

The total system instrumentation and model alignment uncertainty, hereafter referred to as instrumentation uncertainty, is the experimental uncertainty in surface pressure measurement caused by all of the following and their interaction with each other:

• Pressure transducer hysteresis, nonlinearity, thermal sensitivity shift, and thermal zero shift

• Reference pressure accuracy and repeatability

• Analogue amplifier system

• Data digitizing and recording system

• Model pitch, roll and yaw alignment accuracy and repeatability

• In-run variations in freestream Mach number and Reynolds number

• Run-to-run variations in freestream Mach number and Reynolds number

It can be seen from this list that all of these error sources produce random errors, i. e., run-to-run variations in each of these sources is expected. No bias errors in instrumentation uncertainty, e. g., an incorrectly set amplifier gain, can be detected by the present method. The instrumentation uncertainty combines all experimental uncertainty in the entire experiment, except that due to test section flow field nonuniformity and model geometry variation uncertainty. To calculate the instrumentation uncertainty, one compares pressure measurements for the same port from different runs for the model at the same physical location and orientation in the test section. For the same angle of attack, roll angle, flap deflection angle, and axial location, each pair of ports compared will have the same location in the vehicle-induced flow field. When differences in pressure port measurements are made in this way the uncertainty due to flow field nonuniformity and model geometry variation cancels out.

By examining the run summary, Table 2, one chooses run pairs that have the same roll and flap angles and have the same tunnel location. Examples of run pairs that meet these conditions are (20,22), (24,61), (103,112), (42,43), (124, 126), and (131,133). A total of 29 run pairs meet the required conditions. See Ref. 11 for complete details of the uncertainty analysis. For example, port number 1 of the first run listed is compared with port number 1 of the second run listed, port number 2 of the first run is compared with port number 2 of the second run, etc, for each α in common between the two runs. Recall that pressure measurements were obtained for a total of 12 angles of attack for each run; 9 distinct angles of attack and 3 measurements at zero α. As a result, there are a total of 18 combinations of α where pressure comparisons can be made (9 distinct α comparisons plus 9 permutations of zero α measurements). Therefore, an estimate of the total number of pressure port comparisons is

$$(96 \text{ ports}) \times (29 \text{ run pairs}) \times (18 \text{ } \alpha \text{ pairs}) = 50,112 \text{ comparisons}$$

The actual number of comparisons is slightly less than this estimate because some pressure ports were over-scaled for certain conditions. As a result, the total number of pressure port comparisons for instrumentation uncertainty was found to be 48,164.

To make these pressure port comparisons it is required that the α of each of the two runs is identical. If they are not the same, then part of the difference in the two measurements will be due to non-repeatability of α caused by the model pitch mechanism. As mentioned earlier, the pitch control mechanism does not have a feedback control system, that is, a pre-programmed command is given, but the α resulting from the command is precisely achieved. Although the angle of attack read-out is accurate to ± 0.02 deg., the repeatability of the α from one sweep of the mechanism to another can be as large as ± 0.5 deg. For the present experiment, roughly 10 to 20 runs had to be repeated because the resulting α deviated by an excessive value from the nominal α required. None of the angles of attack of all of the runs listed in Table 2 deviates from the nominal value by more than ± 0.28 deg. The average deviation of α from the nominal value for all of the angles of attack of all runs listed in Table 2 was 0.11.

Deviations in α of up to 0.28 deg. run-to-run would introduce an unacceptably large error in the surface pressure uncertainty. To minimize this uncertainty in the analysis, all of the pressure measurements were interpolated to the nominal angles of attack. To accomplish this a cubic spline interpolation was computed for each pressure port as a function of α for each run. The type of cubic spline used was one that minimizes oscillations by adjusting the knot locations and keeping the function values and derivatives at the end points of the interpolation unspecified. The CSKAM subroutine from the IMSL software package (Ref. 20) was used to accomplish the interpolation. Since each run had three separate sets of pressure measurements for zero α, three separate interpolants were computed for each run. As a result, a total of 13,824 interpolants were computed so as to obtain pressure data at precisely the nominal angles of attack. Note that any error caused by interpolation of the data will appear as an additional source of uncertainty in the instrumentation uncertainty, i. e., it will appear as an experimental uncertainty although it is actually a data processing uncertainty.

Now consider how the differences in pressure port measurements are computed. Let the pressure measurement for port i, and angle of attack j be denoted as $\left(\dfrac{p_i}{p_\infty}\right)_j^r$, where the superscript denotes the run number r. Then the average pressure of the port for the two runs being compared is given by

$$\overline{\left(\frac{p_i}{p_\infty}\right)}_j^{r,s} = \frac{1}{2}\left[\left(\frac{p_i}{p_\infty}\right)_j^r + \left(\frac{p_i}{p_\infty}\right)_j^s\right]$$

where $i = 1, 2, ...96$ and $j = 1, 2, ...18$, where 18 is the total number of α's. Let the absolute value of the difference between a pressure measurement and the the average pressure be defined as the residual. Then the residual is given by

$$\left(\frac{\Delta p_i}{p_\infty}\right)_j^{r,s} = \left|\left(\frac{p_i}{p_\infty}\right)_j^r - \overline{\left(\frac{p_i}{p_\infty}\right)}_j^{r,s}\right|$$

Note that the residual can be computed using either the pressure measurement from run r or s.

Test Section Flow Field Nonuniformity Uncertainty

Test section flow field nonuniformity uncertainty is uncertainty in surface pressure measurements caused by the following:

- *Nonuniformity of freestream flow in the test section.* Nonuniformity of flow in the test section can be caused by a number of sources, for example, inaccurately designed or positioned nozzle wall contours, operation of a fixed nozzle wall wind tunnel at a Reynolds number different from the design condition, and slight changes in the location of nozzle wall boundary layer transition due to changing wall temperature. Flow nonuniformity in hypersonic wind tunnels, axisymmetric tunnels especially, is a particularly serious source of uncertainty, but is rarely discussed or documented.

- *Bias errors in the alignment of the model in pitch, roll, and yaw.* Bias errors in pitch and roll could be caused, for example, by an improperly calibrated or used bubble-level to set the pitch and roll angle, an inaccurately leveled test section, or an inaccurate pitch-sector or model positioning system. Yaw angle alignment of the model in the test section is always a difficult measurement to make.

Both of these types of uncertainty are categorized as due to bias errors because they are normally repeatable from run-to-run.

The uncertainty in surface pressure measurement due to a combination of test section flow field nonuniformity uncertainty and instrumentation uncertainty is computed by comparing measurements made at different locations in the test section. The combined flow field nonuniformity and instrumentation uncertainty is calculated by comparing surface pressure measurements for the same port on the body at the same relative location in the vehicle flow field, but at different locations in the test section. This procedure will not include any uncertainty due to model imperfections because by using the same ports for both comparisons, this uncertainty component cancels in taking the difference between the two measurements. The uncertainty due solely to flow field nonuniformity is calculated by statistical methods and will be discussed later.

By examining the run summary, Table 2, for combinations of model axial station, roll angle, and flap deflection angle, one finds four types of run pairs that will produce the types of residuals desired. These are: first, comparisons between measurements made at different axial locations in the test section; second, comparisons between different roll angles at zero α at the same tunnel station; third, comparisons between positive α with a roll angle of 0° and negative α with a roll angle of 180°; and fourth, comparisons between positive α with a roll angle of 90° and negative α with a roll angle of 270°. An example of run pairs for each of these types of comparisons is, respectively, (20,101), (24,32), (35,43), and (46,47).

The total number of pressure port comparisons for these four types, minus the number of comparisons lost due to over-scaled ports, is 101,838 residuals. The residuals for flow field nonuniformity and instrumentation are computed by the same equations given above, but the number of angles of attack, j, for each of the types is different.

Model Geometry Uncertainty

Model geometry uncertainty is uncertainty in surface pressure caused by the following:

• *Model geometry deviations.* These are defined as measurable deviations of the physical model from the conceptual, or mathematical, description of the model. These can be due to a variety of sources, for example, model fabrication deviations such as a non-spherical nose, accidental damage to the model, time-dependent bending distortion due to asymmetric aerodynamic heating, and warpage of the model surface or lifting surfaces due to repeated aerodynamic heating in the test section.

• *Model imperfections.* These are defined as model deviations that are clearly not considered part of the numerical simulation of the physical experiment. Examples of these types of deviations are a poorly fabricated pressure orifice or an orifice that has a burr, and a pressure leak in the fitting or tubing between the pressure orifice and the pressure transducer.

Both of these types of uncertainty sources are categorized as bias errors. One might argue that model geometry deviations, as defined here, should be merged into model imperfections. We respond to that argument by stating that model geometry deviations are simply deviations of the physical model geometry from the mathematical model geometry. If it were desired, the deviations between the physical and mathematical models could be eliminated by a precise inspection of the model and then incorporation of the exact physical model into the mathematical model. This would be an example of incorporating more precise physical boundary conditions into the numerical simulation.

Model geometry uncertainty, along with instrumentation uncertainty, is computed by comparing surface pressure measurements for different ports, but both ports must be at the same physical location in the test section and at the same relative location in the vehicle flow field. This procedure will yield the combined model geometry and instrumentation uncertainty, but will not include any uncertainty due to flow field nonuniformity. Recall that in the previously discussed uncertainty types, pressure port comparisons were always made between the same ports. For those cases, the uncertainty due to model geometry cancels.

The pressure ports on the model that are compared must experience the same flow field. For this to occur, the model, or at least a portion of it, must have at least two planes of mirror symmetry. The present geometry, however, has only one plane of symmetry. Ahead of the slice region of the model, however, there are an infinite number of planes of symmetry because the geometry is axisymmetric. As a result, pressure port comparisons are made only on the conical section of the model. Previous oil flow visualization on the same geometry [7,10] showed that flap deflections of 10 and 20° produced separated flows that did not progress forward of the slice region. Therefore, only run pairs with 0, 10, and 20° flap deflections will be used. To eliminate the possibility of any upstream influence of the slice on the ports used, only axial stations up to 6.2 in. will be considered. This is 1.074 in. ahead of the slice, or about 10 to 20 boundary layer thicknesses.

By examining the run summary, Table 2, for combinations of roll angle, flap deflection angle, and for both runs at the same tunnel station, one finds six types of run pairs which meet the required conditions. All of these run pairs are formed by comparing different roll angles, but each run is for the same flap angle, and the same tunnel location. A complete list of all of the run pairs

and port pairs is given in Ref. 11. The total number of pressure port comparisons for these six types, minus the number of comparisons lost due to over-scaled ports, is 24,196 residuals. The residuals for model geometry and instrumentation are computed by the same equations given earlier.

Uncertainty Results

Plotted in Fig. 8 are all of the residuals computed for instrumentation, flow field nonuniformity, and model geometry uncertainty. It can be seen from Fig. 8 that the magnitude of the uncertainty steadily increases with the magnitude of the pressure measured. This characteristic is typical of experimental instrumentation, and indeed computational predictions. This trend is reduced in the residuals by scaling the residuals with the magnitude of pressure measured. A linear least squares fit of the residuals as a function of average pressure was computed. It was found that the intercept for this least squares fit at zero average pressure was slightly less than zero. As a result, a constrained least squares fit was computed with the intercept set to zero. The resulting fit was computed to be

$$\frac{\Delta p_{ls}}{p_\infty} = 0.00875 \, \frac{p_s}{p_\infty}$$

where p_s is the surface pressure measured. This fit is also shown in Fig. 8.

The sample variance is now calculated with the local sample scaled according to the least squares fit given above. The equation for estimating each type of variance, normalized by the least squares fit of the residuals, is given by

$$\hat{\sigma}^2 = \frac{1}{N} \sum_{k=1}^{N} \left[\frac{\left(\Delta p / p_\infty \right)}{\left(\Delta p_{ls} / p_\infty \right)} \right]_k^2$$

where N is the total number of residuals (or pressure comparisons), and the subscript k indicates the k'th residual. The sample variance due to flow nonuniformity and model geometry can then be calculated from

$$\hat{\sigma}_{flow} = \sqrt{ \hat{\sigma}^2_{flow + instrumentation} - \hat{\sigma}^2_{instrumentation} }$$

$$\hat{\sigma}_{model} = \sqrt{ \hat{\sigma}^2_{model + instrumentation} - \hat{\sigma}^2_{instrumentation} }$$

The total variance due to all of the uncertainty sources is then given by

$$\hat{\sigma}_{total} = \sqrt{ \hat{\sigma}^2_{instrumentation} + \hat{\sigma}^2_{flow} + \hat{\sigma}^2_{model} }$$

Table 3 gives the summary statistics for the uncertainty estimates of the entire experiment. It is seen from the table that the dominant contributor to uncertainty in surface pressure measurement is due to the nonuniformity of the flow field in the test section of the wind tunnel. Although experienced hypersonic wind tunnel experimentalist's have suspected this has been the case, the present statistical analysis quantitatively demonstrates it. Previous force and moment measurements

[7,10] on the same geometry in the same wind tunnel at the same flow field conditions are consistent with the present results. Previous force and moment measurements resulted in contributions of roughly 20% due to instrumentation uncertainty and 80% due to the flow field. The exception to these percentages were in measurement of forebody axial force. This case showed 63% due to instrumentation and 37% due to flow field. The reason for the change in balance is in the inaccuracy in measuring base pressure. Note, in force and moment measurements and the present model geometry, the contribution due to model uncertainty can not be detected.

The dominant contribution of non-uniform flow to uncertainty begs the question; Is this just characteristic of the present wind tunnel, or is it characteristic of other (all) hypersonic wind tunnels? The absolute magnitude, i. e., removing the normalization of the least square fit, of the present results for flow field uncertainty were compared to those for Hypersonic Tunnel B at the Arnold Engineering Development Center [19]. This comparison shows that both wind tunnels are comparable in the magnitude flow field non-uniformity. We contend that the largest contribution to measurement uncertainty in most, if not all, hypersonic wind tunnels is due to flow field non-uniformity. We urge other experimentalists to use the present statistical method to determine if this is the case.

The low contribution of instrumentation uncertainty seen in Table 3 can be used to reevaluate the pressure range chosen for the pressure modules. In the present experiment the pressure range of the PSI modules was chosen to be 0.36 and 1.0 psi differential. This allowed pressures to be measured up to roughly $10.6p_\infty$ and $29.6p_\infty$, respectively, for the two modules. The reason these lower pressure modules were chosen was so that a higher level of pressure sensitivity, and resulting accuracy, could be achieved at the price of having certain pressure ports become over-scaled at larger angles of attack and flap deflections. It can be seen from the uncertainty analysis results that this sacrifice of pressure range for accuracy need not have been made, a tentative conclusion reached in Ref. 16. The statistical results now show conclusively that instrumentation uncertainty, which includes many more components than just the pressure modules, is a factor of 2 lower contributor to uncertainty than flow field nonuniformity.

The total estimated standard deviation of each individual measurement is $\hat{\sigma}_{total} \Delta p_{ls} / p_\infty$. Therefore, the total uncertainty bound on each pressure measurement with probability, or confidence, 95% is

$$\frac{p_s}{p_\infty} \pm 2\hat{\sigma}_{total} \frac{p_{ls}}{p_\infty} = \frac{p_s}{p_\infty} \pm 2\hat{\sigma}_{total} \left(0.00875 \frac{\Delta p_s}{p_\infty}\right)$$

IV. Results and Discussion

The surface pressure measurement results will be discussed in three sections; the conical region of the geometry, in the plane of symmetry on the windward and leeward side of the body, and in the slice region of the body. Recall that only data for the slice configuration, $\delta = 0^o$, is presented in this paper. Complete results are presented in Ref. 11.

In each of the plots in this section, data from all possible runs are plotted together. That is, full advantage is taken of model symmetry, positive and negative angle of attack, and data from both tunnel axial stations are plotted. This strategy is fully consistent with the uncertainty analysis

discussed earlier and, we believe, should be the approach taken when code validation data are presented.

Spherically Blunted Cone

Figure 9 shows the nondimensional surface pressure versus the circumferential angle, θ_w, (measured from the windward ray) for two axial stations and $\alpha = 3^\circ$. The two axial stations, 3.2 in. ($x/r_n = 15.98$), and 5.5 in. ($x/r_n = 25.98$) are two of the three heavily instrumented axial stations on the conical portion of the model. The remaining heavily instrumented station, 7.2 in., was not plotted with the present conical results because it was found that ports 41 and 42 sensed the downstream slice. These two ports were just ahead of the slice by a distance of 0.074 in. and pressure communication occurred in the subsonic portion of the boundary layer. As a result, they could not be considered to represent flow over a spherically blunted cone. Given in the figure title are all run numbers from which data are taken and also the total number of data points plotted in the figure. Figure 9 uses all of the data from the slice-only runs, 16 runs, which yields a total of 1024 pressure measurements plotted in the figure.

Figure 9 shows, as do all of the plots in this section, the trend of high pressure on the windward side and decreasing pressure around the body. There are no surprises here, as this feature has been measured and computed for many years. The purpose of specifically presenting and discussing these body of revolution data is for precise validation of hypersonic CFD codes for laminar boundary layers. The only feature worth noting in Fig. 9 is that the difference in pressures between the $x/r_n = 15.98$ and 25.98, shows that the effect of nose bluntness persists to these axial positions, particularly on the windward side.

Figure 10 shows the surface pressure versus θ_w for an angle of attack of 6°. The data display a similar trend to the result for $\alpha = 3^\circ$, but two differences are noted. First, the difference in pressure levels between the two axial positions has essentially disappeared for this angle of attack. This shows that the effect of nose bluntness has been nearly swallowed in the boundary layer at these axial positions. Second, the pressure is roughly constant on the leeside of the body for $\theta_w > 135^\circ$. The laminar boundary layer on the leeside is probably not separated because $\theta_c/\alpha = 0.6$. Stetson [6] found that the laminar boundary layer sharp cone at $M_\infty = 14$ does not separate until roughly $\theta_c/\alpha = 0.7$. The laminar boundary layer, however, is quite thick on the leeside. This region represents a challenging case to compute because of the nearly separated flow and the interaction of the viscous and adjacent inviscid flow.

Figures 11 and 12 give the surface pressure versus θ_w for angles of attack of 12 and 18°, respectively. For these two angles of attack it is noted that the total number of data points is roughly 40% the number for $\alpha = 3$ and 6°. This is primarily due to the fact that no longer can the negative angles of attack at the beginning of the pitch sweep be plotted by reflecting the data to positive angles of attack. The secondary reason is that a number of ports were over-scaled for these high pressures, e.g., those between $\theta_w = 25$ and 55° for $\alpha = 18^\circ$. It can be seen that the nose bluntness effect at these two axial stations has completed disappeared for these angles of attack. The accurate computation of these leeside flows for large angles of attack is a challenging task. At these angles of attack, there is extensive flow separation on the leeside with strong body vortices interacting with the inviscid flow. There have been a number of numerical solutions published in the literature for blunt cones at large angle of attack. The present measurements will provide a data base for evaluating the accuracy of these calculations.

A comment should be made concerning the relatively large scatter in the data for certain

circumferential angles, most notably for $\alpha = 3^O$. As was discussed in the earlier sections on experimental conditions and uncertainty analysis, this experiment was designed to aggressively detect, and report, as many bias errors in the measurements as possible. This clearly has not been the norm in wind tunnel experimentation. By carefully designing the run schedule, plotting all of the data that can possibly be used, and taking full advantage of model geometry symmetry, we argue that many of the bias errors in an experiment can be converted into random errors. In other words, by plotting the data in this fashion we are able to show what is normally a bias error, such as flow nonuniformity, yaw angle misalignment, and model imperfections, as a random uncertainty on the graph. When all of the individual measurements are taken together, this results in a statistical improvement in measurement accuracy. From fundamental statistics it is known that for random error in N individual measurements the uncertainty bound decreases as $1/\sqrt{N}$.

Sliced Cone: Plane of Symmetry

This section presents the pressures measured in the plane of symmetry of the model, that is, a vertical plane passing longitudinally through the length of the body for a roll angle of 0°. Pressure ports on the slice side of the body are labeled as "Slice Side," and ports on the cone side are labeled "Cone Side." Figure 13 plots the surface pressures, as just described, versus axial distance from the nose tip for an angle of attack of 0°. For the $\alpha = 0^O$ case, data from all of the roll angles tested can be plotted together because the plane of symmetry simply rotates with the roll angle of the body. For non-zero angle of attack, however, a plane of symmetry only exists for roll angles of 0 and 180°. On the conical portion of the body, $x/L < 0.7$, a portion of the classical pressure distribution can be seen. From the stagnation point on the nose, the pressure drop decreases until roughly $x/L = 0.2$. The flow begins to slowly recompress beyond this point. This low pressure region is caused by the adjustment of flow from the nose onto the cone and is referred to as the over-expansion region. For $x/L > 0.6$, the surface pressure on the cone attains a nearly constant value, near that for inviscid flow over a sharp 10° half-angle cone, $p/p_\infty = 3.95$. Although the pressure is near the sharp cone value, a detailed examination of the computed velocity and temperature profiles through the shock layer shows that the nose bluntness effects still remain a large distance from the nose. The distance for entropy swallowing, x_s/r_n, on a spherically blunted cone at zero angle of attack in laminar hypersonic flow has been approximated by Blottner [21] as

$$\frac{x_s}{r_n} \approx \frac{0.05\ Re_{r_n}^{1/3}}{\sin^2 \theta_c}$$

Re_{r_n} is the freestream Reynolds number based on nose radius and θ_c is the cone half-angle. Using this formula for the present case, one obtains a value of $x_s/r_n \approx 54$. At the beginning of the slice $x/r_n = 36.37$ and, as a result, entropy swallowing is occurring over the entire length of the body, even though the cone pressure is near the sharp cone value.

Also seen in Fig. 13 is the decrease in pressure due to the flow expanding over the slice, beginning at $x/L = 0.7$. The pressure drops more slowly than one might expect. This slow drop is due to the three-dimensional character of the flow over the slice, particularly near the beginning of the slice. As the flow expands onto the slice along the hyperbola-shaped edge of the slice, the flow also turns laterally toward the plane of symmetry. This tends to increase the pressure along the plane of symmetry as compared to what a plane two-dimensional, centered expansion would produce. One might suggest that the reason for the relatively slow decrease in pressure is the relaxation of the boundary layer over the beginning portion of the slice. This is, indeed, a factor,

but it is not the dominant factor. An Euler simulation of this flow was computed by Lopez [22] to address this question. She found that this basic character is exhibited in an inviscid solution.

Figure 14 shows the surface pressure versus axial distance for an angle of attack of 3°. All of the data for nonzero angle of attack presented in this section are presented as if the body roll angle is 0°, i. e., the slice is on the windward side of the body for positive angle of attack and on the leeward side for negative angles of attack. An interesting feature to note on this graph is the upstream influence of the slice onto the conical portion of the body and of the base flow onto the slice. Port 41, at a location of $x/L = 0.6929$, is just ahead of the beginning of the slice. In Fig. 14, it can clearly be seen that this port has begun to drop in pressure before the beginning of the slice. The first port on the slice, Port 57, is at a location of $x/L = 0.7025$. Also noted in this figure is the slight decrease in the pressure trend at the last port on the slice, Port 91, at $x/L = 0.9819$. Both of these slight deviations in the pressure trend are due to the thinning of the boundary layer caused by approaching an expansion region. The magnitude of the upstream influence depends on the thickness of the subsonic portion of the boundary layer and the magnitude of pressure change in the expansion. For most angles of attack presented in this section, these upstream effects can be seen at the beginning of the slice and near the base.

Surface pressure versus axial distance for an angle of attack of 15° is shown in Fig. 15. Noted in this figure is the decrease in axial length required for the disappearance of nose bluntness effects. On the windward side, i. e., slice side, the over-expansion region caused by the nose is now completed by roughly $x/L = 0.2$. Recall, for example, at $\alpha = 0^O$ the over-expansion region ended at roughly $x/L = 0.6$. From CFD simulations [22] it is found that the level to which the pressure drops in the over-expansion region, as a percentage of the sharp cone value, actually changes little with angle of attack. The expansion and recompression region, however, occurs over a much smaller axial length for large angles of attack. This makes for a challenging simulation because of the very large axial gradients. On the leeside of the body, i. e., cone side, it is seen that no trace remains of the over-expansion region. As opposed to the windward side, however, it is found that as the angle of attack increases, the over-expansion region disappears on the leeside.

Also noted in Fig. 15 are changes in rate of pressure adjustment over the slice region as compared to lower angles of attack. For this high angle of attack case the pressure is nearly constant over the length of the slice, excluding the region very near the start. At high angle of attack, increasingly strong cross-flow is generated away from the windward plane of symmetry. This counter-acts, and indeed overcomes, the slice-induced flow toward the plane of symmetry discussed earlier. This yields a nearly constant pressure on the slice, similar to what would result from a plane two-dimensional, sharp-cornered, expansion.

Figure 16 shows the surface pressure for an angle of attack of -6°, i. e., the slice is on the leeside of the body and the cone side is to windward. It is seen for this case that the slice has lost much of its effectiveness to expand the flow. For this angle of attack the ratio of pressure ahead of the slice to that near the end of the slice is roughly 2. For $\alpha = 0^O$ (Fig. 13), it is seen that this ratio is about 3.6. One reason for this loss in effectiveness is the thick boundary layer on the leeside shrouding the slice. It is also possible that cross-flow separation occurs at the edge of the slice on the leeside and vortices begin to roll-up along the slice edge.

The surface pressure for an angle of attack of -18° is shown in Fig. 17. Note that no windward side pressures are plotted and, as a result, the pressure scale is greatly expanded. No windward pressures are available because they are all over-scaled. All of these pressure ports were placed on

the low pressure module because for a roll angle of 0° and a large positive angle of attack, they record very low pressures, that is, these ports were optimized to record low pressure values. Results in Fig. 17 are shown because they represent probably the most difficult CFD validation case for the slice only configuration. For this large angle of attack, cross-flow separation and strong leeside body vortices exist. The test for the CFD code is to predict a three-dimensional expansion flow over the slice that is buried in a separated flow and under a vortical flow.

Sliced Cone: Slice Region

This section presents the pressure contours over the slice region and the adjacent region of the cone for a roll angle of 0°. Figure 18 shows the pressure contours for zero angle of attack. Although these types of plots are more qualitative in nature, they help in the physical understanding of the pressure distributions and the flow physics. At each pressure port location shown, the root-mean-square pressure was computed for all pressure measurements taken for the flow condition stated. For example, for Fig. 18 all of the same run numbers were used as given in Fig. 13 yielding a total number of 1920 measurements. Ports that were across the plane of symmetry, Ports 61, 72, and 90 (see Fig. 5), were RMS averaged with their mirror images, Ports 59, 69, and 87, respectively. In the contour plot, mirror symmetry was used across the plane of symmetry to reflect the RMS values to the opposite side of the slice and cone. One final comment is that in the plotting program linear interpolation was used on either rectangular or triangular regions formed by the pressure port locations. Although this technique produces "unrealistic" or "jagged" contours for certain regions, various other numerical techniques proved to be less reliable.

The primary feature that can be seen from Fig. 18 is that the delay in pressure drop on the slice is indeed localized toward the plane of symmetry. The physical explanation for this phenomenon near the plane of symmetry was suggested earlier. The minimum pressure occurs near the edge of the slice on the row of ports near the base of the vehicle. Also note the change in pressure gradient along various rays of the cone that intersect the slice. The least favorable pressure gradient occurs along the plane of symmetry. The most favorable pressure gradient, i. e., the largest magnitude of the rate of pressure decrease, occurs as the edge of the slice approaches tangency to the ray of the cone.

Figures 19 and 20 show the contours of pressure for angles of attack of 9 and 18°, respectively. It can be seen that as the angle of attack increases, the pressure delay effect on the plane of symmetry decreases. Some of the delay effect is seen at $\alpha = 9°$, but at 18°, the pressure is relatively constant across the entire slice. As mentioned earlier, this is due to the increased cross-flow, or up-wash, due to angle of attack. In this regard, an interesting question can be posed: does an angle of attack exist such that a streamline at the edge of the boundary layer experiences both an expansion onto the slice, and also a compression moving off the slice and onto the cone?

Pressure contours for angles of attack of -9 and -18° are shown in Figs. 21 and 22, respectively. Although the pressure levels are very low compared to the slice on the windward side, i. e., positive angles of attack, the contour structure is quite different. For both angles of attack, the counter-rotating, symmetric body vortices above the slice make their presence known on the slice. The pressure in the plane of symmetry is higher than the adjacent region because of the cross-flow stagnation of the vortices. In the plane of symmetry the vortices rotate the flow back toward the surface by way of a three-dimensional spiral vortex pattern. Streamlines on the surface move the fluid away from the plane of symmetry, toward the edge of the slice. A final feature noted is the peculiar contour pattern near the middle of the slice for $\alpha = -18°$, Fig. 22. In the plane

of symmetry, the pressure decreases onto the slice, then very slightly rises, and then slowly drops toward the aft of the slice. One might argue that because of the very low pressures, this is an artifact lost in the uncertainty of the data. Possibly; but one should note that this feature was recorded on all five wind tunnel runs for this case.

VI. Conclusions and Recommendations

An extensive data base of surface pressure measurements for CFD code validation has been produced. This data base, however, covers a very restrictive class of hypersonic flow physics and geometry complexity; perfect gas, laminar flow, spherically blunted cone with an expansion-producing surface. We recommend that additional CFD code validation experiments be conducted for more complex physics, e. g., turbulent flow, and more complex geometries. Surface pressure measurements on the present geometry, except with flap deflections of 10, 20, and 30⁰, will be published in the near future.

The statistical uncertainty analysis employed demonstrated that the dominant contributor to uncertainty in surface pressure measurement is due to the nonuniformity of flow field in the test section of the wind tunnel. Although experienced hypersonic wind tunnel experimentalist's have suspected this has been the case, the present statistical analysis quantitatively demonstrates it. The absolute magnitude of the present results for flow field uncertainty were comparable to those for Hypersonic Tunnel B at the Arnold Engineering Development Center. We contend that the largest contribution to measurement uncertainty in most, if not all, hypersonic wind tunnels is due to flow field non-uniformity. We urge other experimentalists to use the present statistical method to determine if this is the case.

We urge experimental investigators to take a more constructively critical view toward measurements obtained for CFD code validation. They should be willing to identify and quantify components of uncertainty in order to reduce these components and also to allow numerical simulations to aid in improving the quality of the experiment. Likewise, numerical simulations should routinely include error analyses. With the strengths and weaknesses of each approach openly discussed, a more beneficial and productive relationship can be developed in the future.

References

1. Tracy, R. R., "Hypersonic Flow Over a Yawed Circular Cone," GALCIT Memo No. 69, California Inst. of Technology, Pasadena, CA, Aug. 1963.

2. Cleary, J. W., "Effects of Angle of Atttack and Nose Bluntness on the Hypersonic Flow Over Cones," 4th Aerospace Sciences Meeting, AIAA Paper No. 66-414, Los Angles, CA, June 1966.

3. Rainbird, W. J., "Turbulent Boundary-Layer Growth and Sepration on a Yawed Cone," AIAA Journal, Vol. 6, No. 12. Dec. 1968, pp. 2410-2416.

4. George, O. L., Jr., "An Experimental Investigation of the Flow Field Around an Inclined Sharp Cone in Hypersonic Flow," Rept. SS-RR-69-577, Sandia Natl. Labs., Albuquerque, NM, Sept. 1969.

5. Feldhuhn, R. H., Winkelmann, A. E., and Pasiuk, L., "An Eperimental Investigation of the Flow Field Around a Yawed Cone," AIAA Journal, Vol. 9, No. 6, June 1971, pp. 1074-1081.

6. Stetson, K. F., "Boundary-Layer Separation on Slender Condes at Angle of Attack," AIAA Journal, Vol. 10, No. 5, May 1972, pp. 642-648.

7. Oberkampf, W.L., and Aeschliman, D.P., "Joint Computational/Experimental Aerodynamics Research on a Hypersonic Vehicle, Part 1: Experimental Results", AIAA Journal, Vol. 30, No. 8, August 1992, pp. 2000-2009.

8. Walker, M.M., and Oberkampf, W.L., "Joint Computational-Experimental Aerodynamics Research on a Hypersonic Vehicle, Part 2: Computational Results", AIAA Journal, Vol. 30, No. 8, August 1992, pp. 2010-2016.

9. Oberkampf, W.L., Aeschliman, D.P., and Walker, M.M., "Joint Computational and Experimental Research on a Hypersonic Vehicle", AGARD CP514, Theoretical and Experimental Methods in Hypersonic Flows, Paper No. 23, April, 1993.

10. Oberkampf, W.L. Aeschliman, D.P., Tate, R.E., and Henfling, J.F., "Experimental Aerodynamics Research on a Hypersonic Vehicle", Report No. SAND92-1411, Sandia Natl. Laboratories, Albuquerque, NM, April, 1993.

11. Oberkampf, W.L. Aeschliman, D.P., Henfling, J.F., D. E. Larson, and J. L. Payne, "Surface Pressure Measurements for CFD Code Validation in Hypersonic Flow", Sandia National Laboratories, Albuquerque, NM, report in preperation.

12. Hutchinson, M., "Langley Research Center's Hypersonic Wind Tunnel Pressure Instrumentation", Instrument Society of America, Paper No. 91-074, 1991.

13. Chapin, William G., "Dynamic-Pressure Measurements Using an Electronically-Scanned Pressure Module", NASA TM 84650, July 1983.

14. Juanarena, D., "A Modular 64 Channel Pressure Scanner for Aerospace Test", Instrument Society of America, Paper No. 90-160, 1990.

15. Trembley, H., Pressure Systems, Inc., Private Communication, 1993.

16. Aeschliman, D.P., Oberkampf, W.L. , and Henfling, J.F., "Fast-Response, Electronically-Scanned Multi-Port Pressure System for Low-Pressure Hypersonic Wind Tunnel Applications", 18th AIAA Aerospace Ground Testing Conference, Paper No. 94-2580, Colorado Springs, CO, , June 1995.

17. McKee, M.L., "Digital Computer Oriented Methods for Determining the Response of Pressure Measurement Systems to Step and Ramp Forcing Functions", Arnold Engineering Development Center, AEDC-TR-66-225, March 1967.

18. "Aerodynamic Data Accuracy and Quality: Requirements and Capabilities in Wind Tunnel Testing," AGARD CPP-429, Sept. 1987.

19. Oberkampf, W. L., Martellucci, A., and Kaestner, P. C., "SWERVE Surface Pressure Measurements at Mach Numbers 3 and 8 (U)," Rept. No. SAND84-2149, Secret FRD, Sandia Natl Labs., Albquerque, NM, Feb. 1985.

20. "IMSL Math/Library, FORTRAN Subroutines for Mathematical Applications," Vol. 1, Visual Numerics, Inc., Houston, TX.

21. Blottner, F. G., personal communication.

22. Lopez, A. R., personal communication.

DISCLAIMER

Table 1

Mean Wind Tunnel Test Conditions

and Run-to-Run Repeatability (One Standard Deviation)

Flow Parameter	Mean Value	One Standard Deviation	One Standard Deviation (percent)
Freestream Mach No.	7.841	±0.0025	0.032
Stagnation Pressure	358.6 psia	±7.7 psia	2.1
Stagnation Temperature	1139 R	±24 R	2.1
Freestream Static Pressure	0.0416 psia	±0.0006 psia	1.4
Freestream Unit Reynolds No.	2.096×10^6 /ft.	$±0.077 \times 10^6$ /ft.	3.7

Table 2

Run Schedule

Forward Tunnel Station, 7.6 in.

Roll Angle (deg)	$\delta = 0^o$	$\delta = 10^o$	$\delta = 20^o$	$\delta = 30^o$
0	20, 22, 62	42, 43	48, 49	56, 57
90	24, 26, 59, 61	37, 39	46	54
180	30, 32, 58	35, 36	44, 45	50, 53
270	28, 29	40, 41	47	55

Aft Tunnel Station, 4.1 in.

Roll Angle (deg)	$\delta = 0^o$	$\delta = 10^o$	$\delta = 20^o$	$\delta = 30^o$
0	101, 102	118, 119	124, 126	131, 133
180	103, 112	115, 116	122, 123	127, 129

Table 3

Summary of Surface Pressure Uncertainty Analysis

Source of Uncertainty	No. of Residuals	Normalized $\hat{\sigma}$	% of Total RMS Uncertainty
Instrumentation	48,164	0.56	12
Flow Field	101,838	1.28	64
Model	24,196	0.79	24
Total	174,198	1.60	100

Figure Titles

Figure 1: Photograph of the Wind Tunnel with Test Section Open

Figure 2: Schematic of Wind Tunnel Model

Figure 3: Longitudinal Cross-Section of Wind Tunnel Model

Figure 4: Highly Instrumented Conical Stations
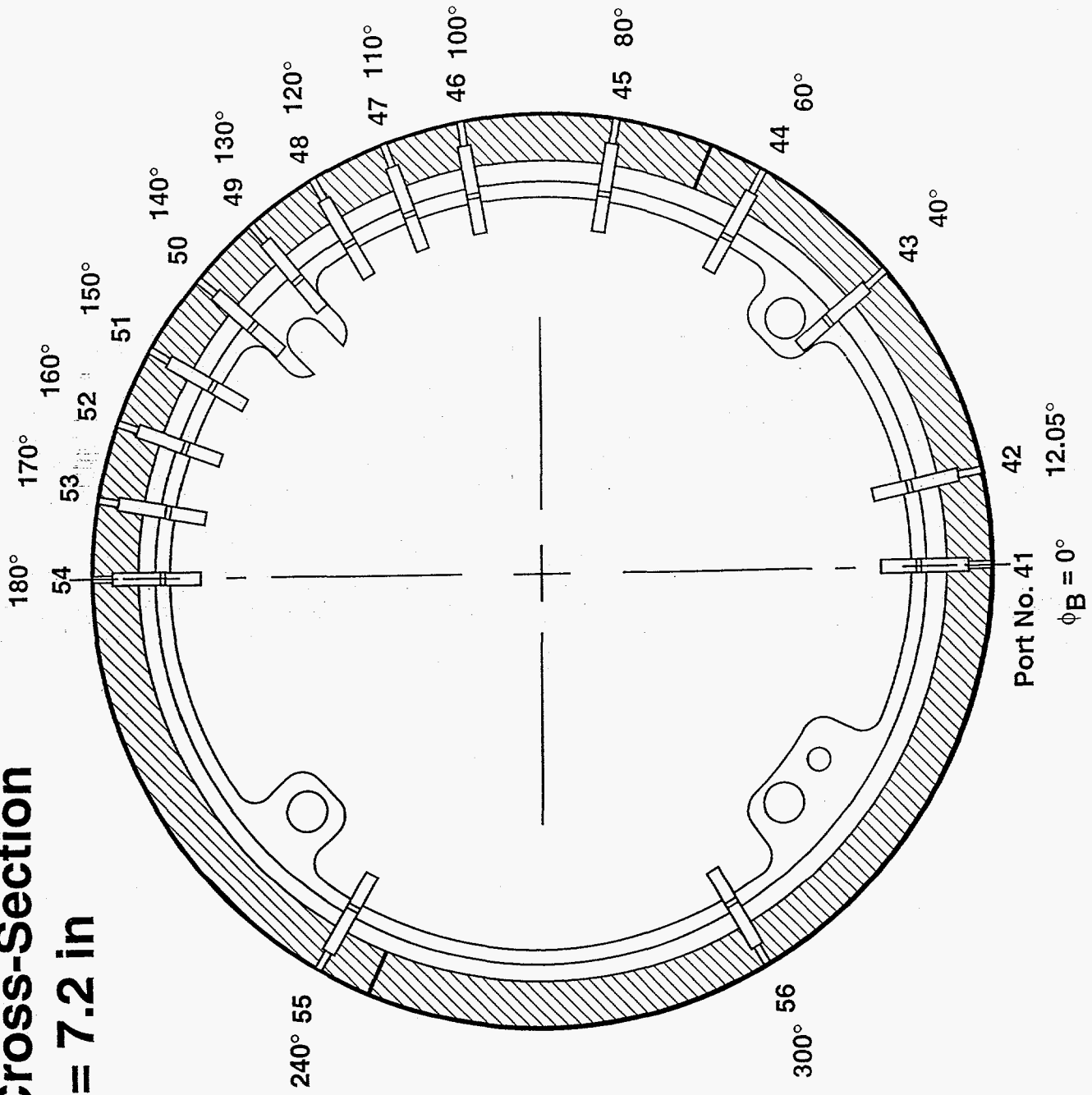
Figure 5: Pressure Port Locations in the Slice/Flap Region

Figure 6: Base Cover Extension, Sting, and Sting Cover

Figure 7: Photograph of Model with One of Two Pressure Modules Installed

Figure 8: Combined Instrumentation, Flow Field, and Model Residuals versus Pressure Magnitude

Figure 9: Surface Pressure versus Circumferential Angle for $\alpha = 3^o$ (Runs 20, 22, 62, 24, 26, 59, 61, 30, 32, 58, 28, 29, 101, 102, 103, 112; 1024 measurements)

Figure 10: Surface Pressure versus Circumferential Angle for $\alpha = 6^o$ (Runs 20, 22, 62, 24, 26, 59, 61, 30, 32, 58, 28, 29, 101, 102, 103, 112; 1024 measurements)

Figure 11: Surface Pressure versus Circumferential Angle for $\alpha = 12^o$ (Runs 20, 22, 62, 24, 26, 59, 61, 30, 32, 58, 28, 29, 101, 102, 103, 112; 403 measurements)

Figure 12: Surface Pressure versus Circumferential Angle for $\alpha = 18^o$ (Runs 20, 22, 62, 24, 26, 59, 61, 30, 32, 58, 28, 29, 101, 102, 103, 112; 355 measurements)

Figure 13: Surface Pressure in the Plane of Symmetry for $\alpha = 0^o$ (Runs 20, 22, 62, 24, 26, 59, 61, 30, 32, 58, 28, 29, 101, 102, 103, 112; 1152 measurements)

Figure 14: Surface Pressure in the Plane of Symmetry for $\alpha = 3^o$ (Runs 20, 22, 62, 30, 32, 58, 101, 102, 103, 112; 240 measurements)

Figure 15: Surface Pressure in the Plane of Symmetry for $\alpha = 15^o$ (Runs 20, 22, 62, 101, 102; 120 measurements)

Figure 16: Surface Pressure in the Plane of Symmetry for $\alpha = -6^o$ (Runs 20, 22, 62, 30, 32, 58, 101, 102, 103, 112; 240 measurements)

Figure 17: Surface Pressure in the Plane of Symmetry for $\alpha = -18^o$ (Runs 30, 32, 58, 103, 112; 75 measurements)

Figure 18: Surface Pressure in the Slice Region for $\alpha = 0^o$

Figure 19: Surface Pressure in the Slice Region for $\alpha = 9^o$

Figure 20: Surface Pressure in the Slice Region for $\alpha = 18^{\circ}$

Figure 21: Surface Pressure in the Slice Region for $\alpha = -9^{\circ}$

Figure 22: Surface Pressure in the Slice Region for $\alpha = -18^{\circ}$

Fig. 1

Three Flaps
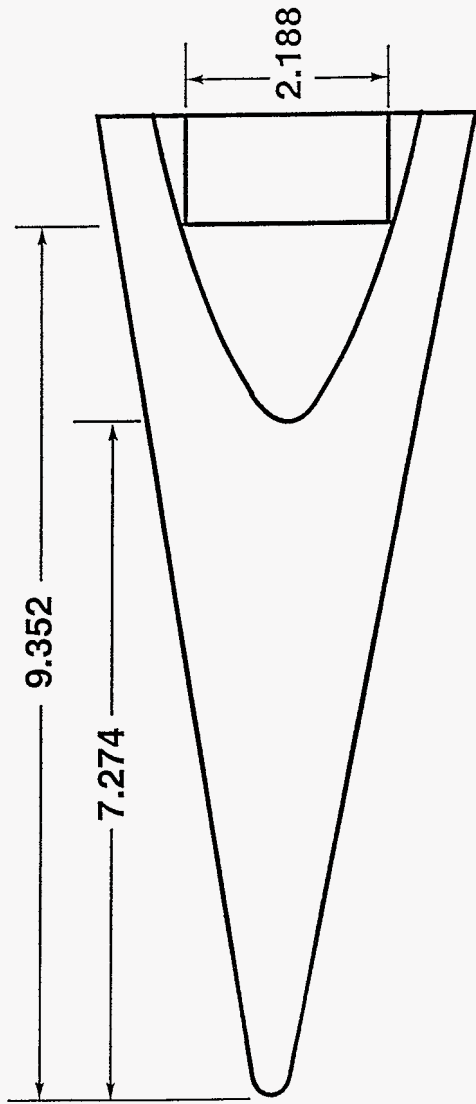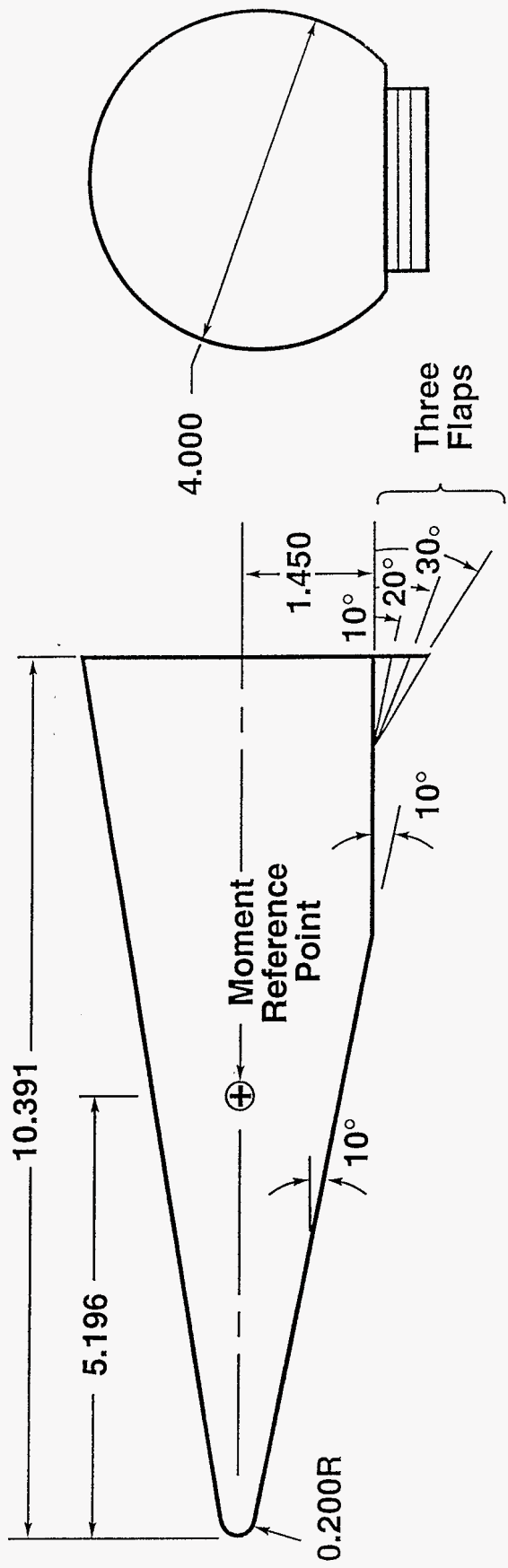
All Dimensions in Inches

4.000

1.450

10°
20°
30°

10°

Moment
Reference
Point

⊕

10°

10.391

5.196

0.200R

2.188

9.352

7.274

Fig. 2

TA0267.04.02

Fig.3

Cross-Section of Model

Base Cover and Sting

Sting Cover

Section 4

O-Ring

Section 3

O-Ring

K7

T4 78

66

54

40

Section 2

O-Ring

36

22

Section 1

O-Ring

T2 18

4

2

K9

Nose Tip

1

Pressure Port Nos.

3

T1 5

Assembly Screw (3)

21

23

Assembly Screw (3)

39

K5 41 57 58 62 67 T3 73 79

Assembly Screw (3)

84

91

O-Rings

Flap (30° shown)
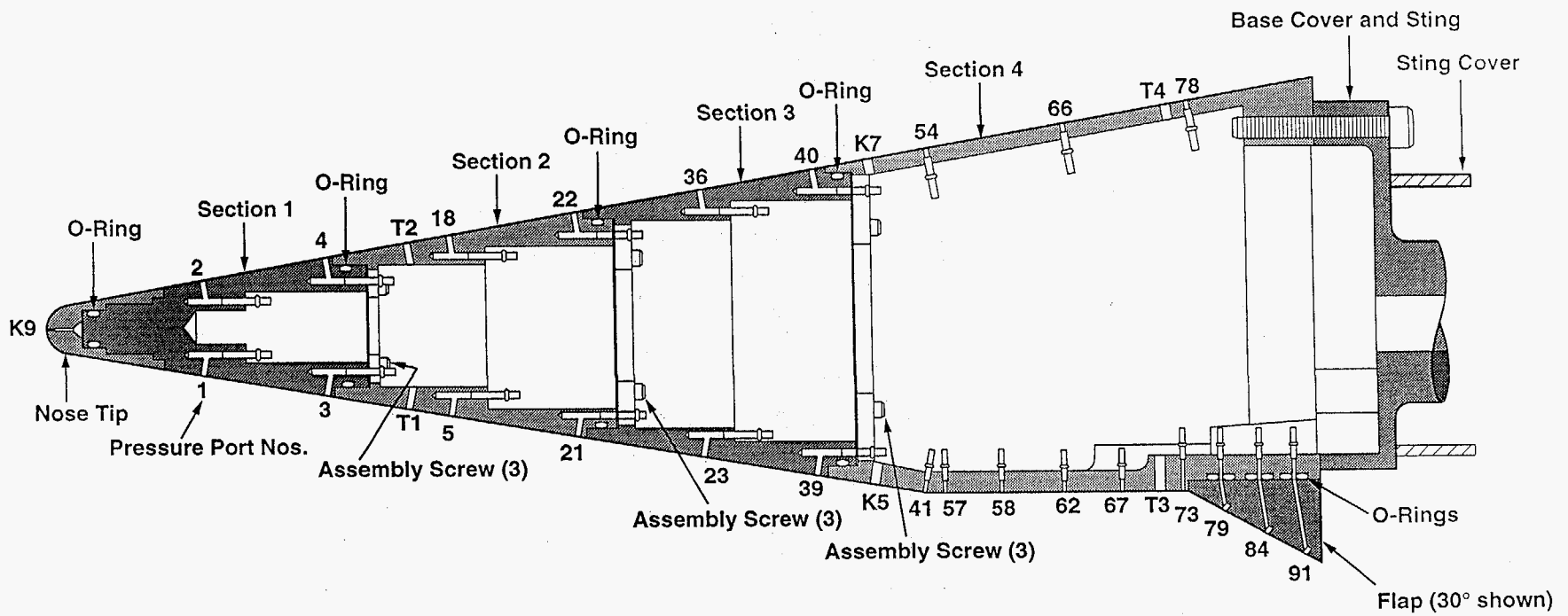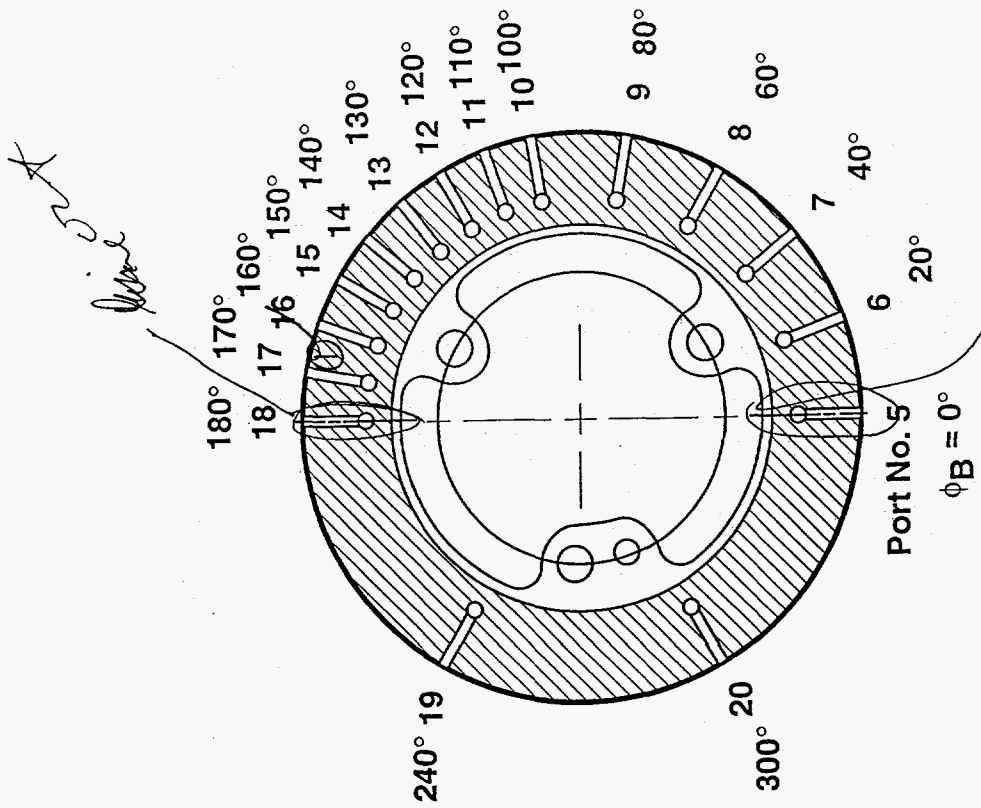
Model Cross-Section
x = 3.2 in

Fig. 4a
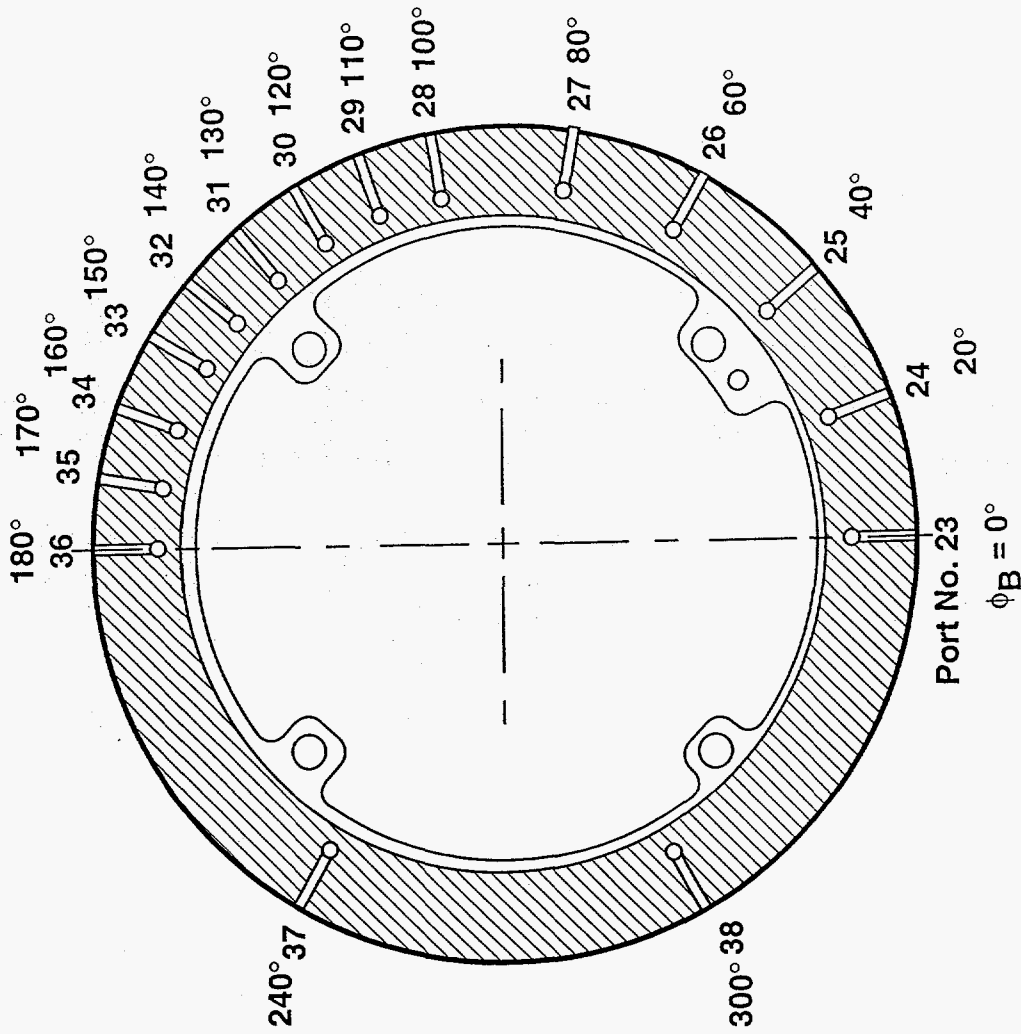
Model Cross-Section
x = 5.2 in

$Fig. 46$

Port No. 23
$\phi_B = 0°$

180° 36
170° 35
160° 34
150° 33
140° 32
130° 31
120° 30
110° 29
100° 28
80° 27
60° 26
40° 25
20° 24

240° 37
300° 38

Model Cross-Section
x = 7.2 in

Fig. 4c

180° 54
170° 53
160° 52
150° 51
140° 50
130° 49
120° 48
110° 47
100° 46
80° 45
60° 44
40° 43
42
12.05°
Port No. 41
φB = 0°

240° 55
300° 56

T371K CH9213.01

Fig.5

Pressure Port Locations in the Slice/Flap Region

Fig. 6

Sting and Sting Cover

1.251   3.60

Model Base

2.46

Section A-A

A

2.375

Sting Cover

Sting

.625

10.135
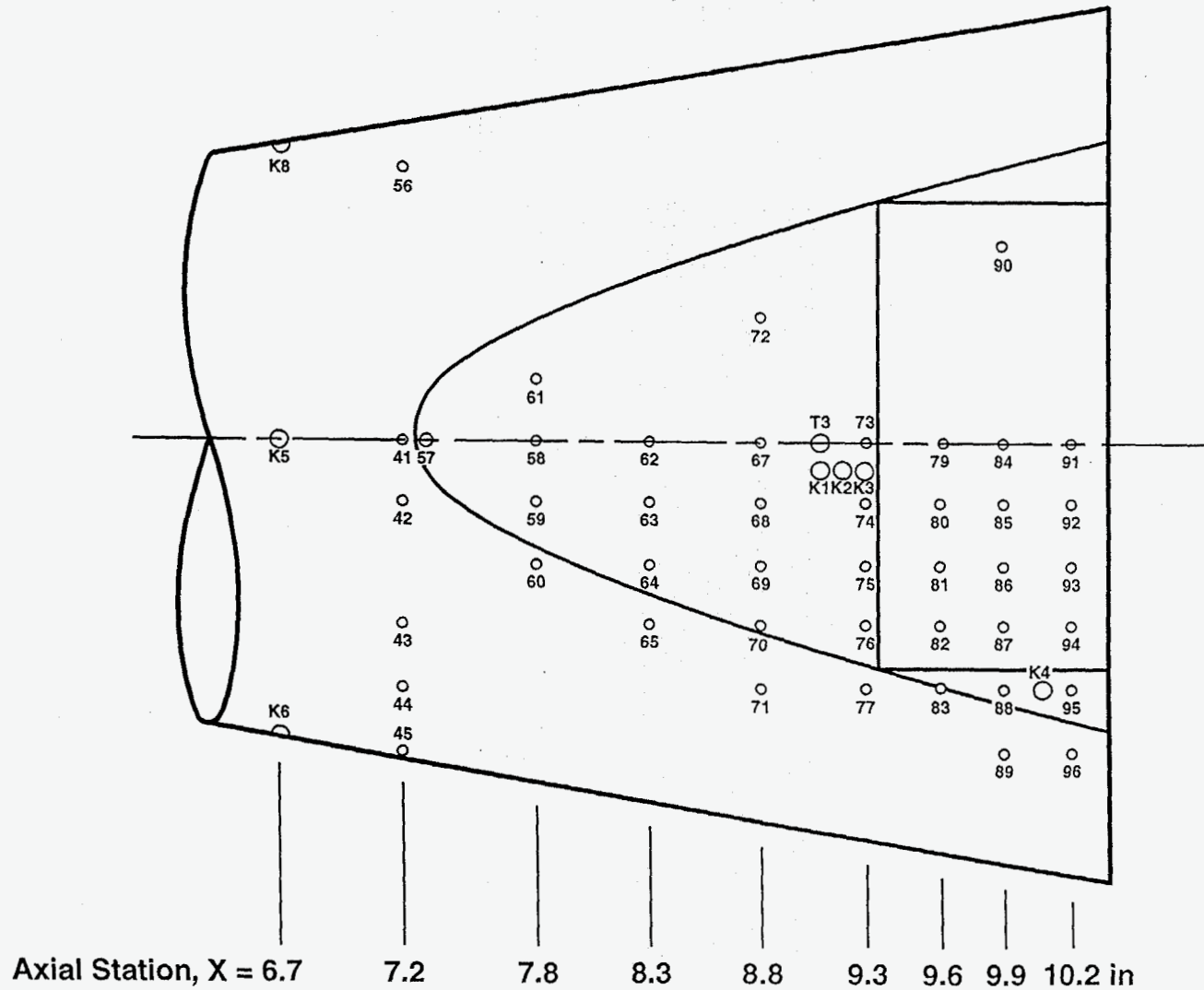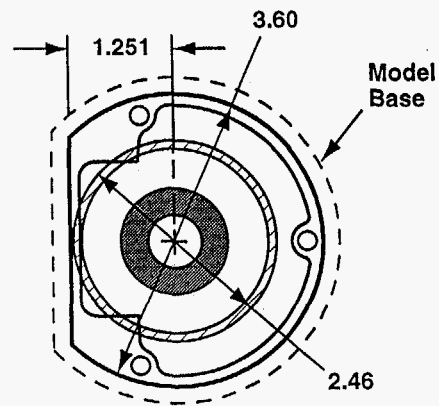
A
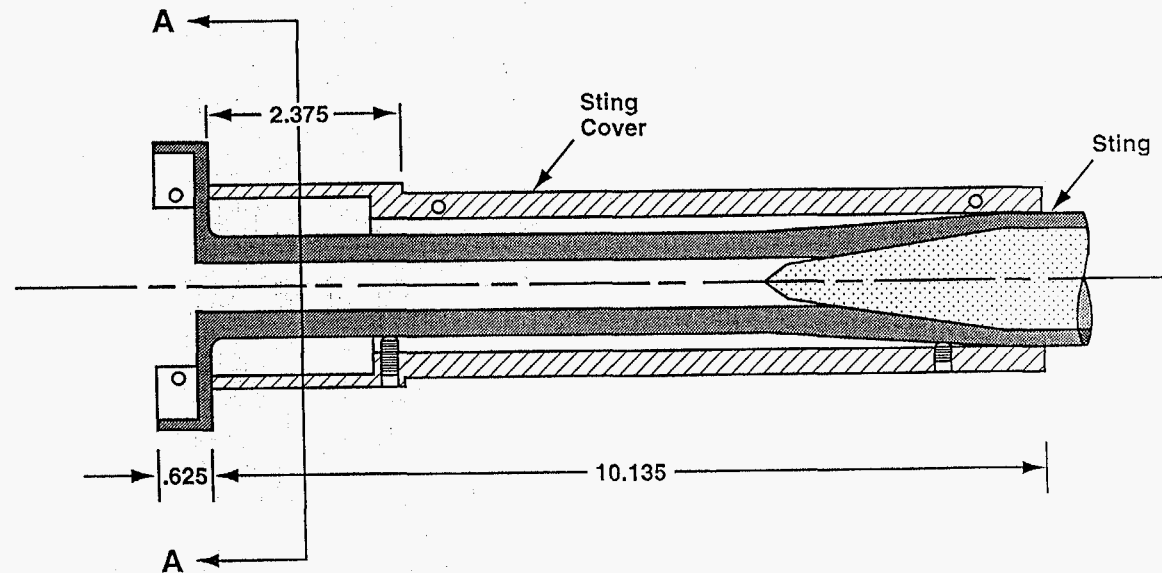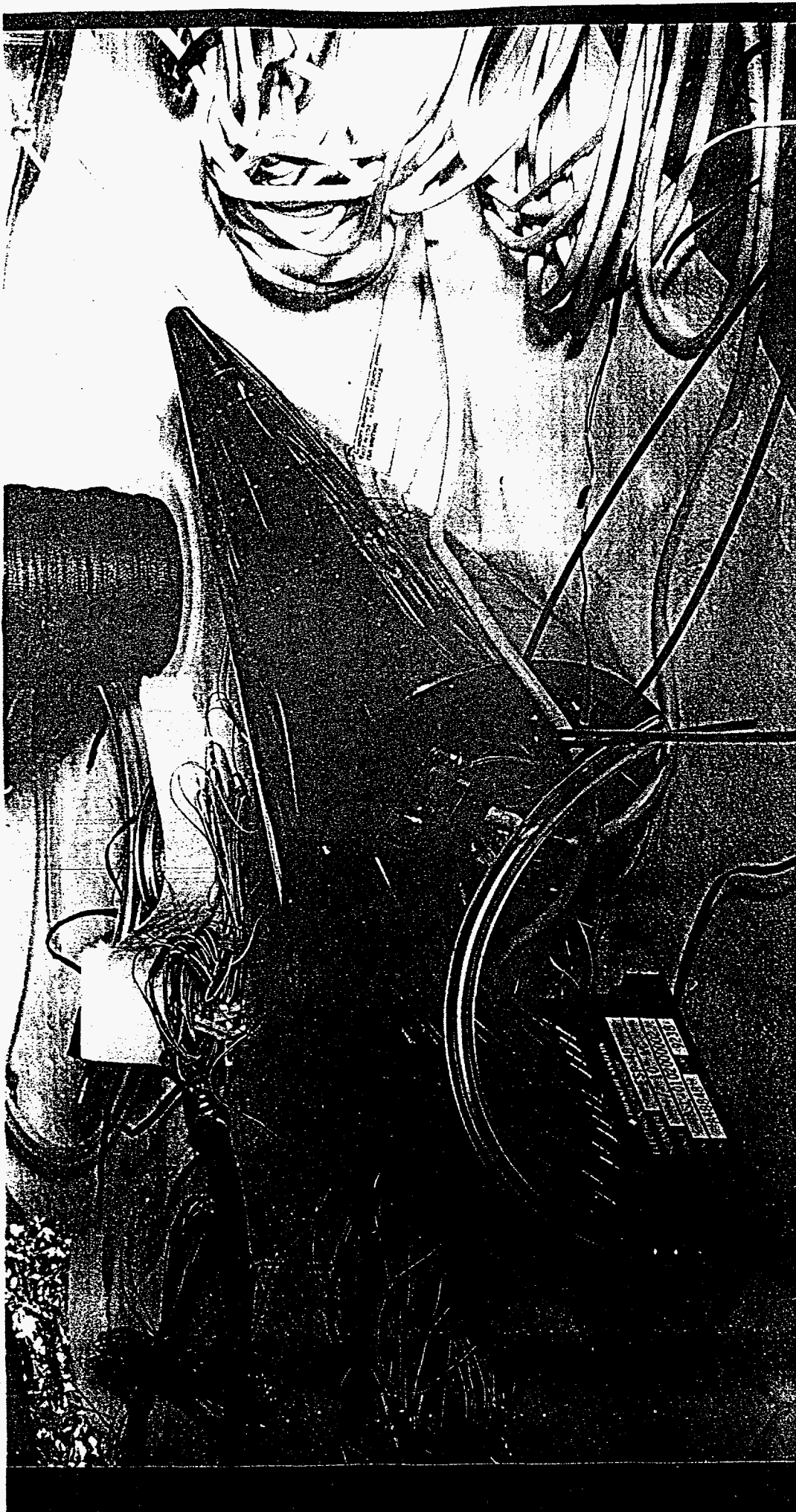
Fig. 7

Fig. 8

Combined Instrumentation, Flow Field
and Model Uncertainty
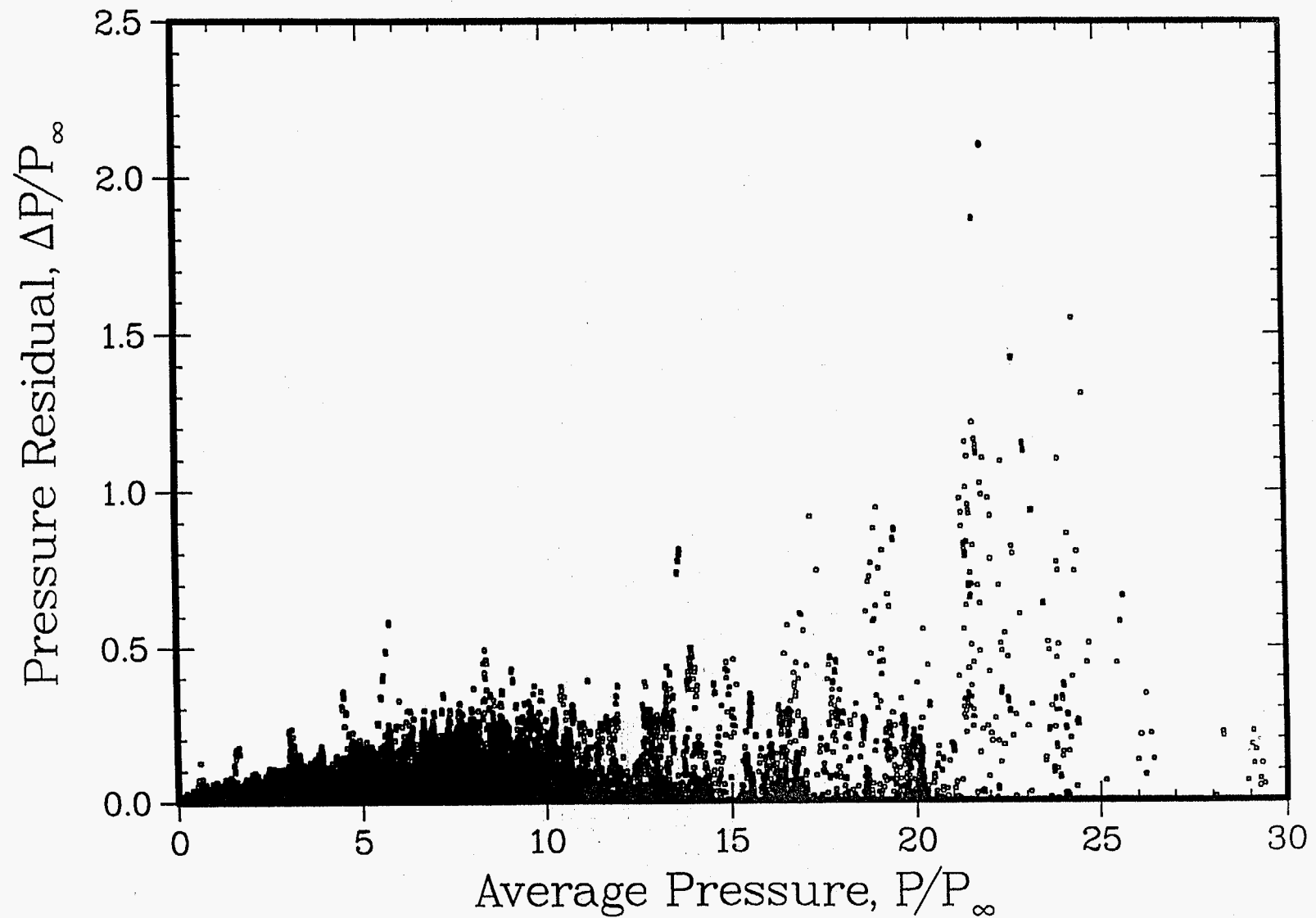
Fig. 9

Total Points per Curve = 512, Skipped points: Curve 1 = 0, Curve 2 = 0
Run Numbers: 20 22 24 26 28 29 30 32 58 59 61 62 101 102 103 112

$\alpha = 3.00°$

Legend:
- ○ $X/R_n = 15.98$
- □ $X/R_n = 25.98$

Y-axis: P/P_∞

X-axis: θ_W (deg)

Fig. 10

Total Points per Curve = 512, Skipped points: Curve 1 = 0, Curve 2 = 0
Run Numbers: 20 22 24 26 28 29 30 32 58 59 61 62 101 102 103 112

$\alpha = 6.00°$

Legend:
- ○ $X/R_n = 15.98$
- □ $X/R_n = 25.98$

Axes: P/P_∞ (vertical), θ_W (deg) (horizontal)
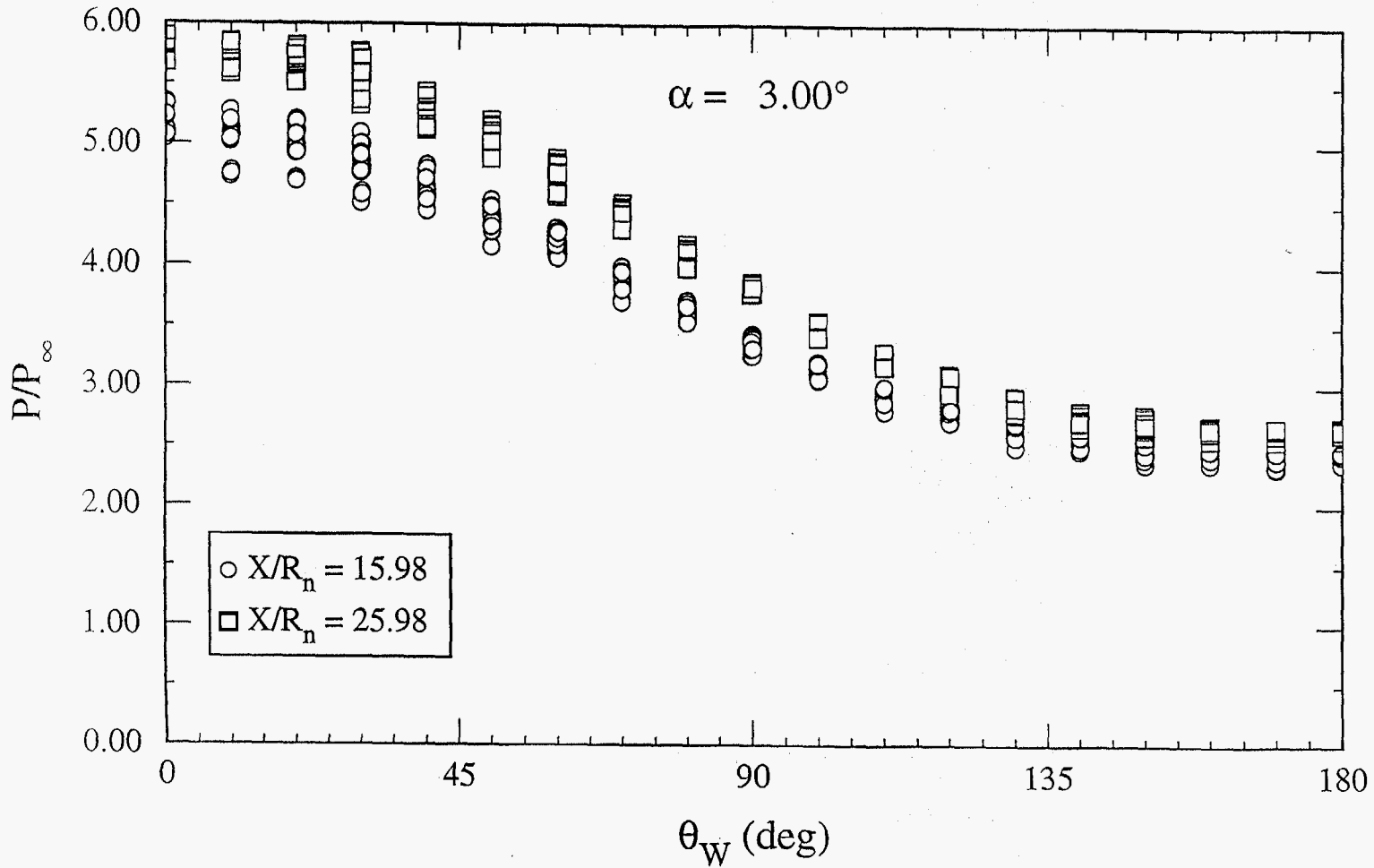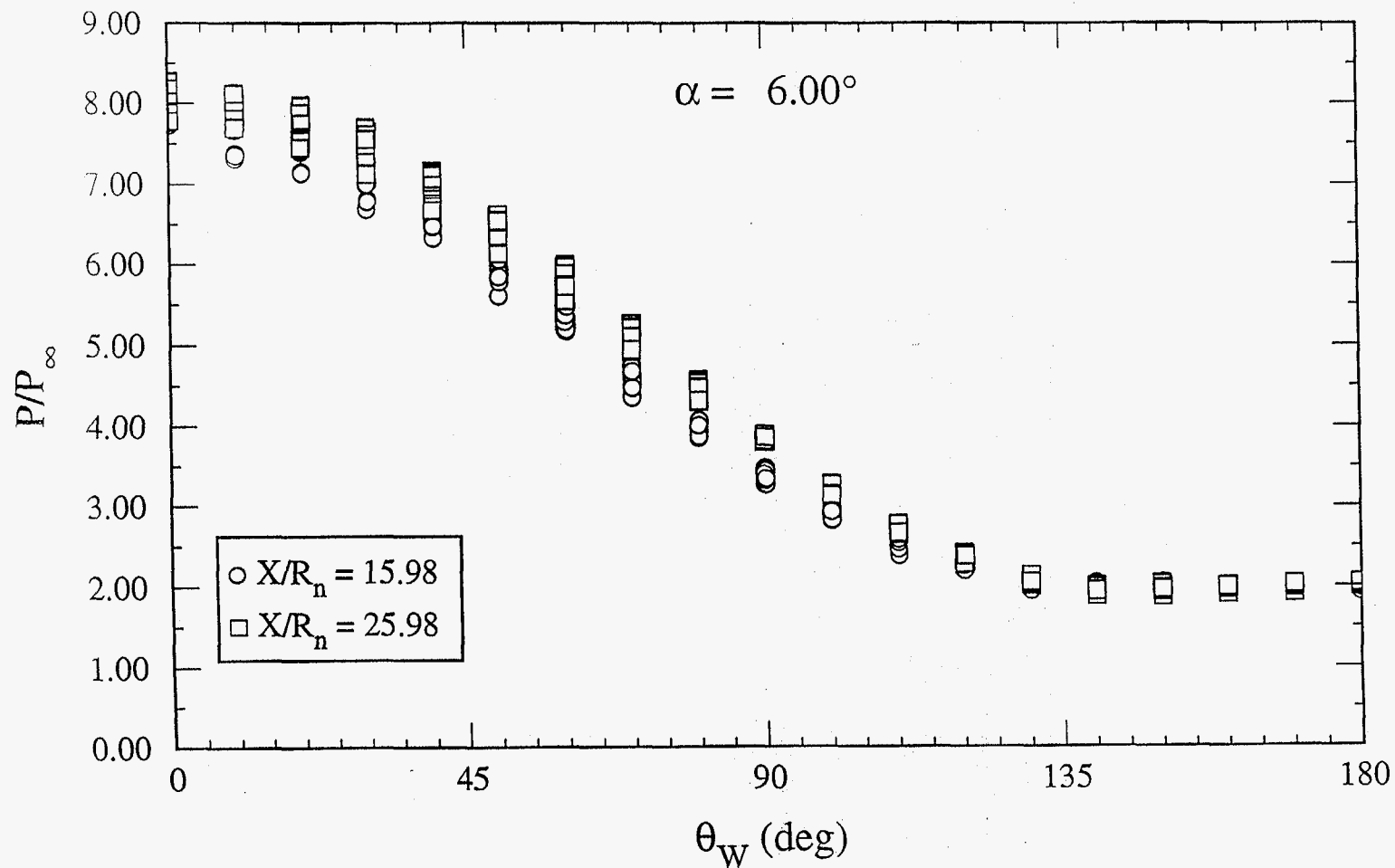
$Fig. 11$

Total Points per Curve = 256, Skipped points: Curve 1 = 52, Curve 2 = 57
Run Numbers: 20 22 24 26 28 29 30 32 58 59 61 62 101 102 103 112

$\alpha = 12.00°$

Legend:
- o $X/R_n = 15.98$
- □ $X/R_n = 25.98$

Y-axis: P/P_∞

X-axis: θ_W (deg)
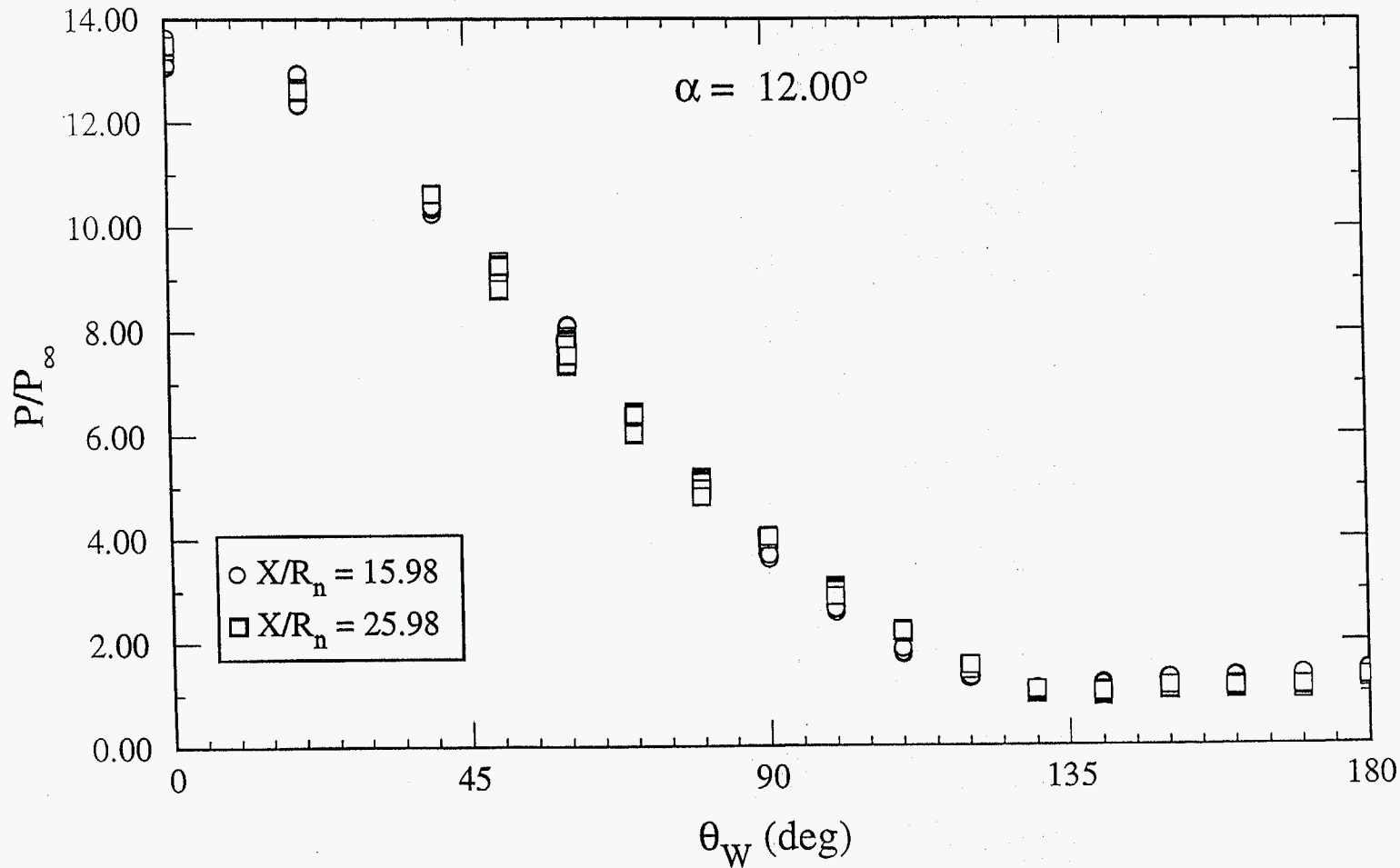
F_{19}, $/2$

Total Points per Curve = 256, Skipped points: Curve 1 = 80, Curve 2 = 77
Run Numbers: 20 22 24 26 28 29 30 32 58 59 61 62 101 102 103 112

$\alpha = 18.00°$

θ_W (deg)

P/P$_\infty$

○ X/R$_n$ = 15.98
□ X/R$_n$ = 25.98
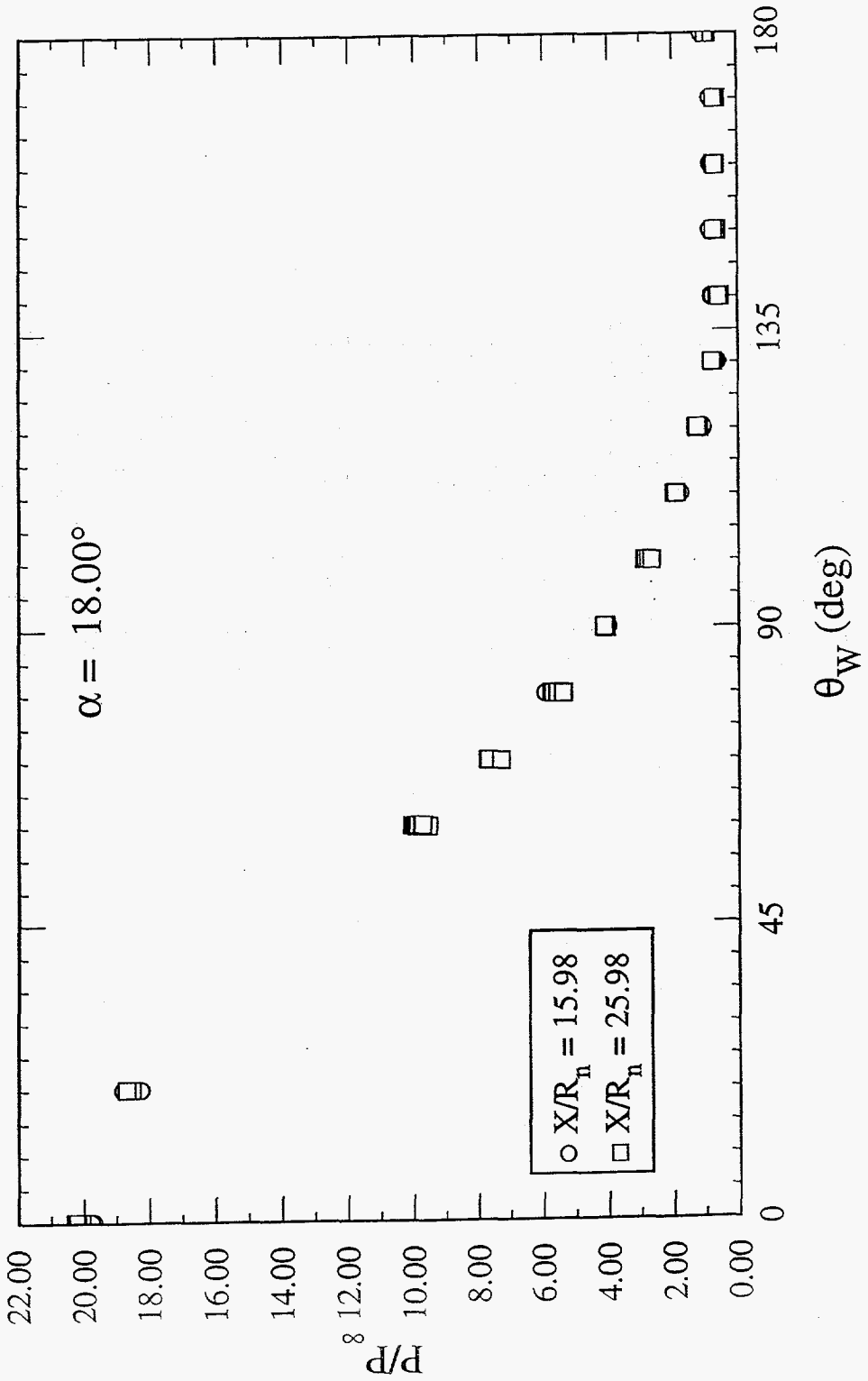
Fig. 13

$\delta = 0.00°$, Curve1: Total=720, Skipped=0, Curve2: Total=432, Skipped=0
Run Numbers: 20 22 24 26 28 29 30 32 58 59 61 62 101 102 103 112
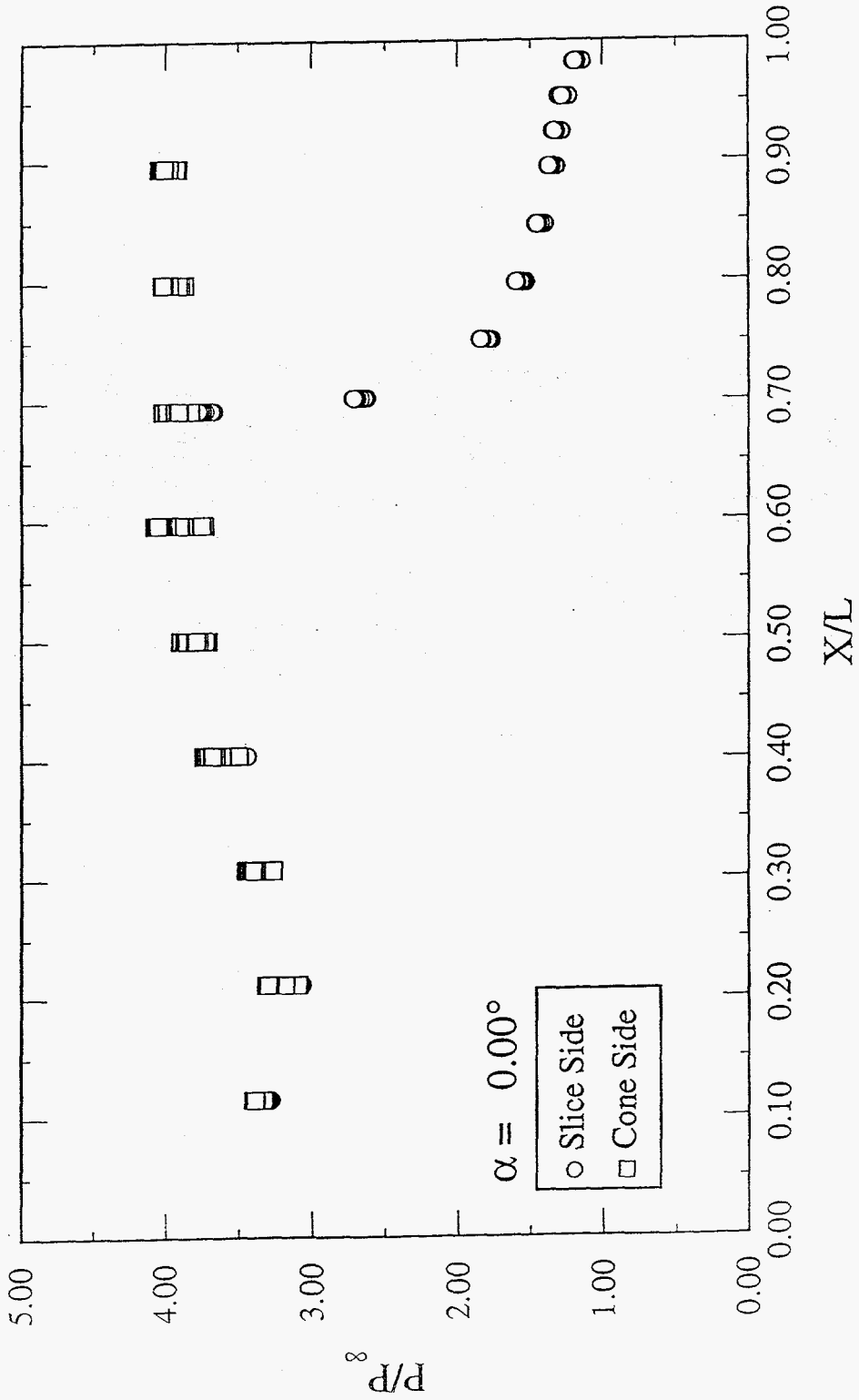
Fig. 14

$\delta = 0.00°$, Curve1: Total=150, Skipped=0, Curve2: Total=90, Skipped=0
Run Numbers: 20 22 62 101 102 30 32 58 103 112

$\alpha = 3.00°$

○ Slice Side
□ Cone Side

X/L

P/P_∞

6.00
5.00
4.00
3.00
2.00
1.00
0.00

0.00 0.10 0.20 0.30 0.40 0.50 0.60 0.70 0.80 0.90 1.00
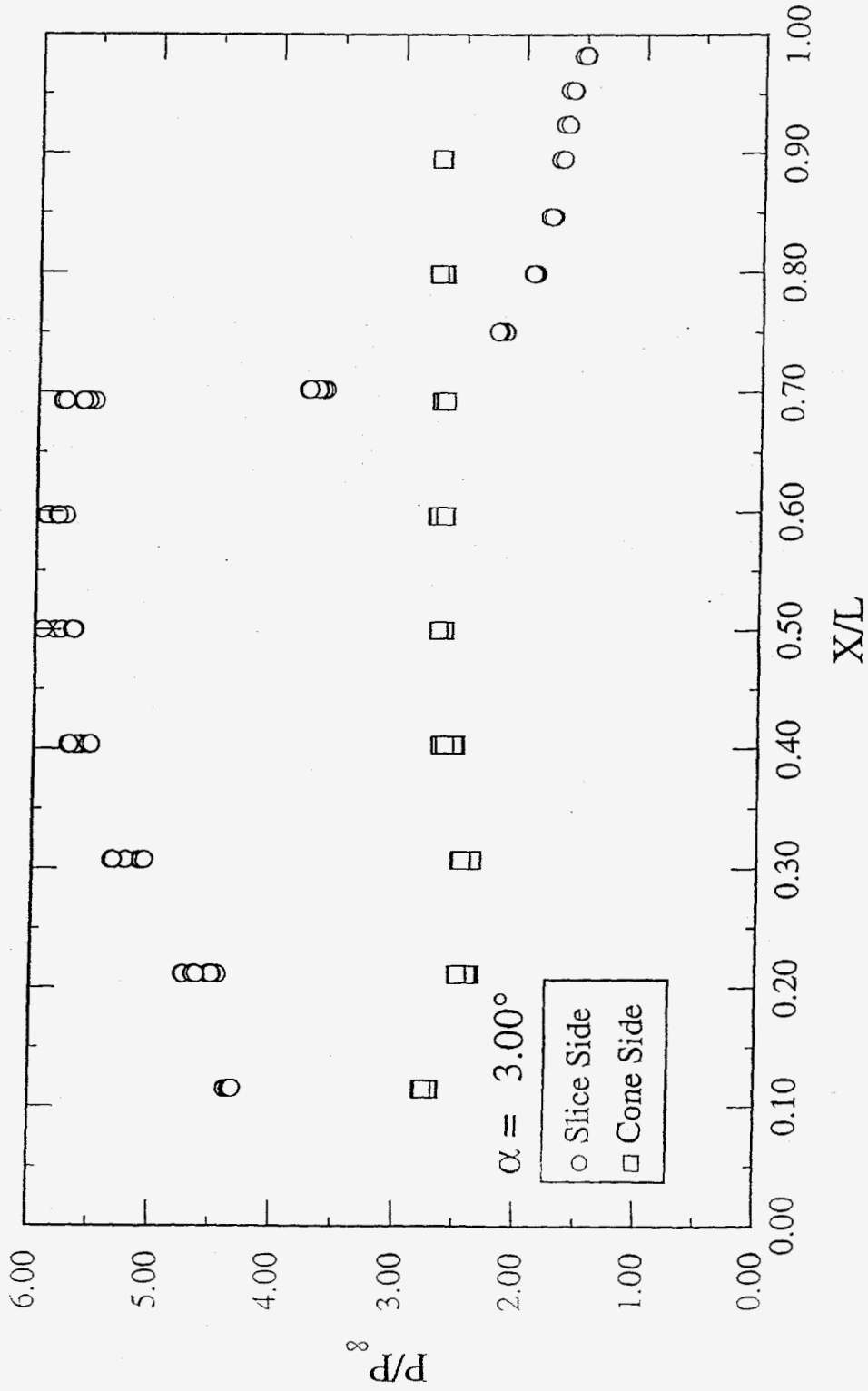
$F_{19.15}$

$\delta = 0.00°$, Curve1: Total=75, Skipped=0, Curve2: Total=45, Skipped=0
Run Numbers: 20 22 62 101 102
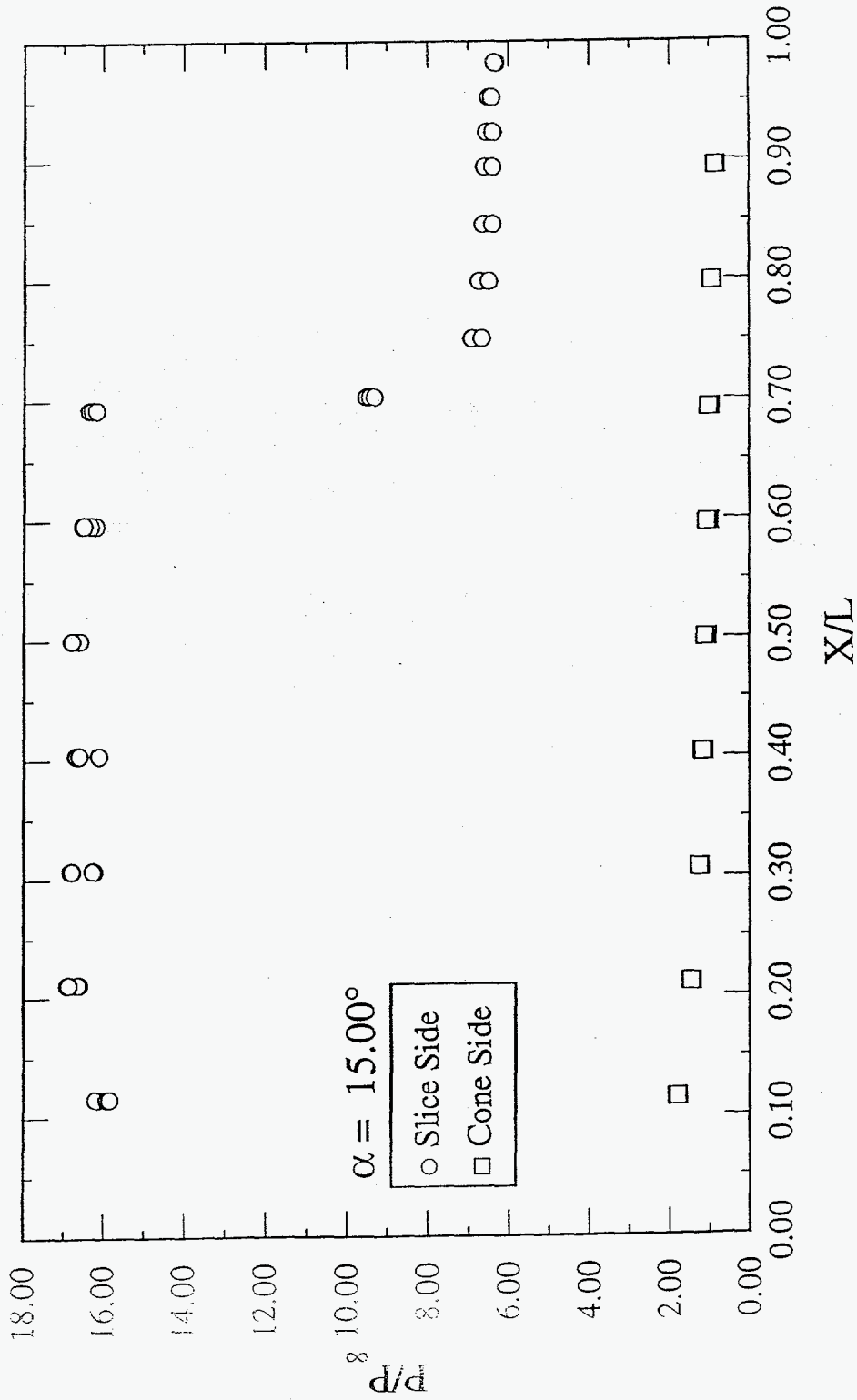
X/L

P/p

$\alpha = 15.00°$

○ Slice Side
□ Cone Side

Fig. 16

$\delta = 0.00°$, Curve1: Total=150, Skipped=0, Curve2: Total=90, Skipped=0
Run Numbers: 20 22 62 101 102 30 32 58 103 112

$\alpha = -6.00°$

○ Slice Side
□ Cone Side

P/P_∞

X/L
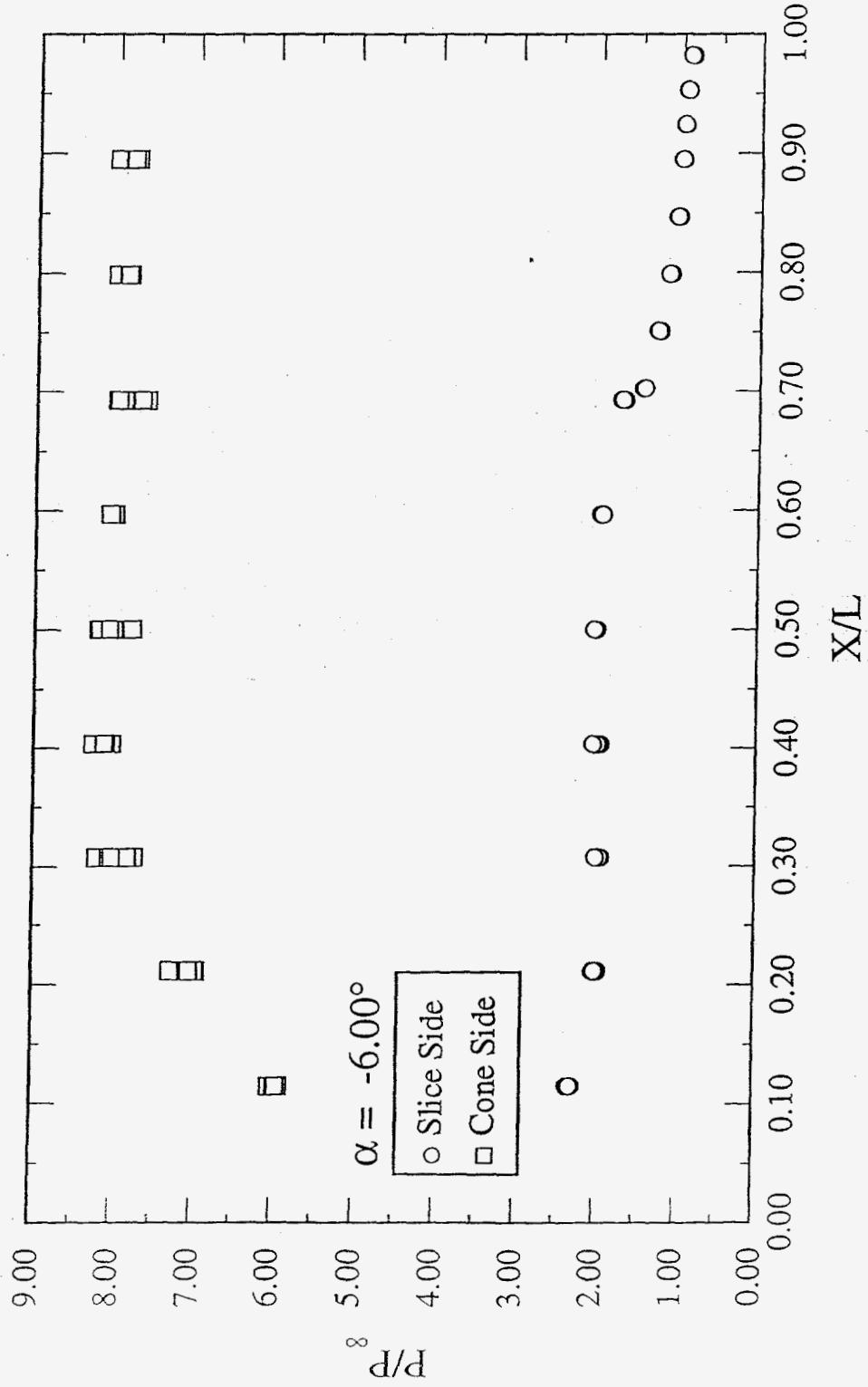
$F_{ig}.17$

$\delta = 0.00°$, Curve1: Total=75, Skipped=0, Curve2: Total=45, Skipped=45

Run Numbers: 30 32 58 103 112

$\alpha = -18.00°$

○ Slice Side

X/L

P/P_∞

Fig. 18

(3D) I Print I 5 Jun 1995 I ly3 I0 conf0 alpha 0 pl geom0 pl I 20 22 24 26 28 29 30 32 58 59 61 62 101 102 103 I 2:*d = 0-0

$\alpha = 0.00°$

3.00
1.00
1.25
1.50
3.50
1.75
2.25
3.00
2.50
3.75

Y
X
Z

$F_{19.19}$

Y

Z ⌐ X

$\alpha = 9.0°$

2.20

3.20

7.20

3.20

8.20

5.20

6.20

9.20

7.20

Fig. 20

(3D) | Print | 5 Jun 1995 | ty3_t0 cont0 alpha_18p1 geom0 pit | 20 22 62 101 t02

$\alpha = 18°$

Fig. 21

Y

X

Z

$\alpha = -9.0°$

0.40
0.30
0.50
0.60
0.50
1.30
0.50
0.70
0.80
0.90
1.10
1.20

Fig. 22

$\alpha = -18°$